The Astrophysical Journal, 983:30 (28pp), 2025 April 10 https://doi.org/10.3847/1538-4357/ada608

EPOCHS. I. The Discovery and Star-forming Properties of Galaxies in the Epoch of Reionization at $6.5 < z < 18$ with PEARLS and Public JWST Data

Christopher J. Conselice[1], Nathan Adams[1], Thomas Harvey[1], Duncan Austin[1], Leonardo Ferreira[2], Katherine Ormerod[1,3], Qiao Duan[1], James Trussler[1], Qiong Li[1], Ignas Juodžbalis[1,4,5], Lewi Westcott[1], Honor Harris[1], Louise T. C. Seeyave[6], Asa F. L. Bluck[7], Rogier A. Windhorst[8], Rachana Bhatawdekar[9], Dan Coe[10], Seth H. Cohen[8], Cheng Cheng[11,12], Simon P. Driver[13], Brenda Frye[14], Lukas J. Furtak[15], Norman A. Grogin[16], Nimish P. Hathi[16], Benne W. Holwerda[17], Rolf A. Jansen[8], Anton M. Koekemoer[16], Madeline A. Marshall[18], Mario Nonino[19], Aaron Robotham[13], Jake Summers[8], Stephen M. Wilkins[20], Christopher N. A. Willmer[21], Haojing Yan[22], and Adi Zitrin[15]

[1] Jodrell Bank Centre for Astrophysics, University of Manchester, Oxford Road, Manchester M13 9PL, UK; conselice@manchester.ac.uk
[2] Department of Physics & Astronomy, University of Victoria, Finnerty Road, Victoria, British Columbia, V8P 1A1, Canada
[3] Astrophysics Research Institute, Liverpool John Moores University, 146 Brownlow Hill, Liverpool, L3 5RF, UK
[4] Kavli Institute for Cosmology, University of Cambridge, Madingley Road, Cambridge, CB3 OHA, UK
[5] Cavendish Laboratory - Astrophysics Group, University of Cambridge, 19 JJ Thomson Avenue, Cambridge, CB3 OHE, UK
[6] Astronomy Centre, University of Sussex, Falmer, Brighton BN1 9QH, UK
[7] Stocker AstroScience Center, Dept. of Physics, Florida International University, 11200 S.W. 8th Street, Miami, FL 33199, USA
[8] School of Earth and Space Exploration, Arizona State University, Tempe, AZ 85287-1404, USA
[9] European Space Agency (ESA), European Space Astronomy Centre (ESAC), Camino Bajo del Castillo s/n, 28692 Villanueva de la Cañada, Madrid, Spain
[10] AURA for the European Space Agency (ESA), Space Telescope Science Institute, 3700 San Martin Drive, Baltimore, MD 21218, USA
[11] Chinese Academy of Sciences South America Center for Astronomy, National Astronomical Observatories, CAS, Beijing 100101, People's Republic of China
[12] 2 CAS Key Laboratory of Optical Astronomy, National Astronomical Observatories, Chinese Academy of Sciences, Beijing 100101, People's Republic of China
[13] International Centre for Radio Astronomy Research (ICRAR) and the International Space Centre (ISC), The University of Western Australia, M468, 35 Stirling Highway, Crawley, WA 6009, Australia
[14] University of Arizona, Department of Astronomy/Steward Observatory, 933 N Cherry Avenue, Tucson, AZ85721, USA
[15] Department of Physics, Ben-Gurion University of the Negev, P.O. Box 653, Be'er-Sheva 84105, Israel
[16] Space Telescope Science Institute, 3700 San Martin Drive, Baltimore, MD 21218, USA
[17] Department of Physics and Astronomy, University of Louisville, 102 Natural Sciences Building, Louisville, KY 40292, USA
[18] National Research Council of Canada, Herzberg Astronomy & Astrophysics Research Centre, 5071 West Saanich Road, Victoria, BC V9E 2E7, Canada; & ARC Centre of Excellence for All Sky Astrophysics in 3 Dimensions (ASTRO 3D), Australia
[19] INAF-Osservatorio Astronomico di Trieste, Via Bazzoni 2, I-34124 Trieste, Italy
[20] Astronomy Centre, Department of Physics and Astronomy, University of Sussex, Brighton, BN1 9QH, UK
[21] Steward Observatory, University of Arizona, 933 N Cherry Avenue, Tucson, AZ, 85721-0009, USA
[22] Department of Physics and Astronomy, University of Missouri, Columbia, MO 65211, USA
Received 2024 July 20; revised 2024 December 18; accepted 2024 December 23; published 2025 April 2

Abstract

We present in this paper the discovery, properties, and a catalog of 1165 high-redshift $6.5 < z < 18$ galaxies found in deep JWST NIRCam imaging from the GTO PEARLS survey combined with data from JWST public fields. We describe our bespoke homogeneous reduction process and our analysis of these areas including the NEP, CEERS, GLASS, NGDEEP, JADES, and ERO SMACS-0723 fields with over 214 arcmin^2 imaged to depths of ∼30 mag. We describe our rigorous methods for identifying these galaxies, involving the use of Lyman-break strength, detection significance criteria, visual inspection, and integrated photometric redshift probability distributions predominately at high redshift. Our sample is a robust and highly pure collection of distant galaxies from which we also remove brown dwarf stars, and calculate completeness and contamination from simulations. We include a summary of the basic properties of these $z > 6.5$ galaxies, including their redshift distributions, UV absolute magnitudes, and star formation rates. Our study of these young galaxies reveals a wide range of stellar population properties as seen in their colors and SED fits, which we compare to stellar population models, indicating a range of star formation histories (SFHs), dust, active galactic nuceli, and/or nebular emission. We find that a strong trend exists between stellar mass and $(U - V)$ color, as well as the existence of the "main-sequence" of star formation for galaxies as early as $z \sim 12$. This indicates that stellar mass, or an underlying variable correlating with stellar mass, is driving galaxy formation, in agreement with simulation predictions. We also discover ultra-high-redshift candidates at $z > 12$ in our sample and describe their properties. Finally, we note a significant observed excess of galaxies compared to models at $z > 12$, revealing a tension between predictions and our observations.

Unified Astronomy Thesaurus concepts: Extragalactic astronomy (506); Galaxy evolution (594)

Materials only available in the online version of record: machine-readable table

1. Introduction

The study of high-redshift galaxies has, since the 1990s, been one of the most active areas of astrophysical research, providing critical insights into the early Universe and the formation and

evolution of galaxies (e.g., M. Castellano et al. 2022; N. J. Adams et al. 2023; H. Atek et al. 2023; S. L. Finkelstein et al. 2023; P. Chakraborty et al. 2024). The earliest galaxies likely formed within 100 million years of the Big Bang, and these objects represent the building blocks of the Universe, as they are the seeds of the structures we observe today. These distant galaxies are furthermore of particular interest because they are thought to have been shaped by different physical processes than those that govern the evolution of galaxies in the present-day Universe. This can then lead to a new understanding for how the first large structures in the Universe were assembled. However, finding these systems and separating them from contaminants has remained a major problem that has long plagued this field (e.g., N. J. Adams et al. 2023; P. Arrabal Haro et al. 2023a).

Multiple research groups in the past 30 yr have utilized the Hubble Space Telescope (HST) to identify galaxies at redshifts higher than $z \sim 6$ by employing the well-established technique of identifying absorption caused by neutral hydrogen through the Lyman-break method. Before JWST, astronomers identified tens of thousands of galaxies beyond a redshift of $z = 4$ (corresponding to 10% of the age of the Universe, $\sim$1.5 Gyr), and individual galaxy candidates were known to exist as early as $z \sim 10$ (e.g., R. J. Bouwens et al. 2011, 2016; D. J. McLeod et al. 2016; P. A. Oesch et al. 2018; B. Salmon et al. 2018; T. Morishita et al. 2018; M. Stefanon et al. 2019; R. A. A. Bowler et al. 2020; Y. Harikane et al. 2022). A redshift of $z \sim 8.5$ marks a significant threshold beyond which sources start to "drop out" in the HST *Y*-band (F105W) and *J*-band (F125W) filters, making it a notable frontier for this type of work pre-JWST (R. J. Bouwens et al. 2011; R. S. Ellis et al. 2013; P. A. Oesch et al. 2014; Y. Harikane et al. 2022).

A primary goal of JWST is to push the redshift frontier and search for galaxies that host the first generation of stars when the Universe was <5% of its current age. Since the launch of JWST on Christmas Day of 2021, there have been many studies with claims for measuring and finding the most distant galaxies in the Universe at redshifts higher than the limit achievable with HST (e.g., M. Castellano et al. 2022; C. T. Donnan et al. 2023; N. J. Adams et al. 2023; S. L. Finkelstein et al. 2023, 2024; H. Atek et al. 2023; H. Yan et al. 2023; Y. Harikane et al. 2023; D. Austin et al. 2023; G. C. K. Leung et al. 2023; C. J. Willott et al. 2023; D. J. McLeod et al. 2024). While many of these galaxy candidates have yet to be verified with spectroscopy at their measured photometric redshifts, it is clear that we have entered a new epoch of extragalactic astronomy, which may lead us to discover the first stars, black holes, and galaxies (e.g., J. A. A. Trussler et al. 2022a; A. Nabizadeh et al. 2024). Based on these galaxies, we hope to be able to answer questions regarding the formation and evolution of the first objects, their dark matter halos, as well as potentially cosmological properties.

Since the release of the first deep JWST images, there are now many deep and independent fields in which to find the most distant galaxy candidates to measure their properties (e.g., A. C. Carnall et al. 2022; C. T. Donnan et al. 2023; N. J. Adams et al. 2023; P. G. Pérez-González et al. 2023). These early observations from JWST data suggest the possible presence of a significantly higher number of galaxies than initially anticipated, particularly during the epoch of reionization, or potentially even earlier at cosmic dawn. These very early results demonstrate that we are finding candidate galaxies at redshifts upward of $z > 12$ (e.g., N. J. Adams et al. 2023; M. Castellano et al. 2022; C. T. Donnan et al. 2023; R. P. Naidu et al. 2022; N. J. Adams et al. 2023; H. Atek et al. 2023; H. Yan et al. 2023). Some of these galaxies have possible confirmed spectroscopic redshifts (E. Curtis-Lake et al. 2022; B. Wang et al. 2023; M. Castellano et al. 2024; S. Carniani et al. 2024; J. A. Zavala et al. 2024) using NIRSpec and MIRI observations, while others are convincingly shown to be contamination from lower redshifts (e.g., P. Arrabal Haro et al. 2023a).

JWST clearly allows us to probe galaxies at a greater depth in the near- and mid-infrared than previously missions (e.g., HST, the Spitzer Space Telescope, and the VISTA Telescope). The increased resolution, depth, and general higher image fidelity of JWST allows features such as the Lyman-break and the rest-frame UV spectral energy distributions (SEDs) of galaxies with redshifts greater than $z > 9$ to be observed. This provides insights into not only the redshifts of these systems but also their stellar masses and star formation rates (SFRs). However, to accurately study these galaxies, we must ensure that we are finding and identifying correctly these systems with minimal contamination.

While the GTO teams (e.g., M. Castellano et al. 2022; A. J. Bunker et al. 2023; D. J. Eisenstein et al. 2023; K. N. Hainline et al. 2024a) and others have studied these fields for the most part in this way already, with the exception of the NEP field, we discuss here as part of our GTO program PEARLS, we have carried out this meta-analysis constructing a new reduction and sample construction for a few reasons. We give this program and sample the name: "Observing the First Epochs of Galaxy Assembly and Reionization" (EPOCHS). One goal of EPOCHS is to carry out research on a large area of the sky with the same reductions, galaxy detection, and analysis processes. As different reductions can, and nearly always do, lead to different high-redshift galaxy samples constructed, a consistent method will allow for a better understanding of biases and the determination of random and systematic errors. We also combine all of these data to limit the effects of cosmic variance, given that many of these fields are small, and thus any results derived from one or a few of them are to some degree biased by the narrow area of the sky observed (see, e.g., B. P. Moster et al. 2011; C. Kragh Jespersen et al. 2024).

In this paper we present the results of our search for $z > 6.5$ galaxies within 11 of the deepest JWST fields observed to date, including our GTO time as part of the PEARLS project (R. A. Windhorst et al. 2022). This also includes the public GLASS, NGDEEP, JADES, CEERS, JADES, and the SMACS-0723 fields. In this paper, we explore the properties of 1165 galaxies that were discovered at these early epochs. We describe this sample, which is used throughout the other papers in this series, including the construction of the UV luminosity and stellar mass functions (N. J. Adams et al. 2024; T. Harvey et al. 2024). As part of this goal, in this paper we describe the basic features of this large collection of distant galaxies in terms of their galaxy luminoisities, colors, star formation rates, as well as their redshift distributions and number densities.

Other papers in the EPOCHS series include a measurement of the early UV luminosity function (LF; EPOCHS II; N. J. Adams et al. 2024), the β slopes and star formation rates for these systems (EPOCHS III; D. Austin et al. 2024), and how stellar masses are distributed depending on certain stellar population models used (EPOCHS IV; T. Harvey et al. 2024), as well as morphology (C. J. Conselice et al. 2024), and size evolution (K. Ormerod et al. 2024). We have also studied the

Table 1
List of Our Observed Fields and the Depths and Areas of Each, Adapted from a Version of This Table from T. Harvey et al. (2024)

Field	Area (arcmin^2)	HST/ACS_WFC		JWST/NIRCam								
		F606W	F814W	F090W	F115W	F150W	F200W	F277W	F335M	F356W	F410M	F444W
NEP	57.32	28.74	⋯	28.50	28.50	28.50	28.65	29.15	⋯	29.30	28.55	28.95
El Gordo*	3.90	⋯	⋯	28.23	28.25	28.18	28.43	28.96	⋯	29.02	28.45	28.83
MACS-0416*	12.3	⋯	⋯	28.67	28.62	28.49	28.64	29.16	⋯	29.33	28.74	29.07
Clio*	4.00	⋯	⋯	28.12	⋯	28.07	28.21	28.68	⋯	28.91	⋯	28.71
CEERS	66.40	28.6	28.30	⋯	28.70	28.60	28.89	29.20	⋯	29.30	28.50	28.85
CEERSP9	6.08	28.31	28.32	⋯	29.02	28.55	28.78	29.20	⋯	29.22	28.50	29.12
SMACS-0723*	4.31	⋯	⋯	28.75	⋯	28.81	28.95	29.45	⋯	29.55	⋯	29.28
GLASS	9.76	⋯	⋯	29.14	29.11	28.86	29.03	29.55	⋯	29.61	⋯	29.84
NGDEEP HST-S	1.28	29.20	28.80	⋯	29.78	29.52	29.48	30.28	⋯	30.22	⋯	30.22
NGDEEP HST-D	4.03	30.30	30.95	⋯	29.78	29.52	29.48	30.28	⋯	30.22	⋯	30.22
JADES Deep GS	22.98	29.07	⋯	29.58	29.78	29.68	29.72	30.21	29.58	30.17	29.64	29.99

Note. The values listed include the unmasked areas and depths of the observations for this paper, which are also used in other EPOCHS papers. The depths listed are at 5σ in AB magnitudes, measured in 0.″16 radius apertures. Where depths are tiered across mosaics (e.g., HST ACS/WFC observations in the Hubble Ultra Deep Field, HUDF, Parallel 2), we have listed the depths and areas separately. The four spokes of the NEP time-domain field (TDF) and 10 CEERS pointings have uniform depths (within 0.1 mags) with the exception of CEERS pointing-9 (P9), which we list separately. Areas are given in arcmin^2 and measured from the mask to account for the masked areas of the image and unused cluster modules. Fields with an "*" indicate that we have excluded the NIRCam module containing a lensing cluster from our analysis.

MIRI properties of some of our sample (Q. Li et al. 2024a), as well as investigated how our samples varies as a function of environment, and how many of our systems are in overdensities (Q. Li et al. 2024b). This particular paper is the introduction to this series and describes our methodology, our completeness calculations, and the basic properties of the $z > 6.5$ galaxies we have discovered.

The ultimate understanding of the role of galaxies in the early Universe, including at the epoch of reionization, will require building up large samples at these redshifts. Studies such as these are the first step in this process with JWST, which will ultimately address fundamental questions for how reionization occurred, and when and how the first galaxies assembled. The advantage of our study is that we combine several of the deepest available fields to study the very first galaxies with NIRCam and the HST. This allows us to determine how galaxy selection depends on field and filters as well as create a large sample for meta analyses.

The structure of the remainder of this paper is as follows. In Section 2, we describe the PEARLS and public deep field observations and our observational program, focusing on the NIRCam observations, which we have reprocessed, as well as the data products derived from this new data set. In Section 2.3, we describe the selection procedure undertaken to define a robust sample of galaxies with redshifts $z > 6.5$. We present an analysis of the completeness using our procedures and describe the properties of the galaxies we have found in Section 3. We present a discussion of this sample's properties in Section 4, while a summary of our findings is included in Section 5. Throughout this work, we assume a standard cosmology with $H_0 = 70\,\mathrm{km\,s^{-1}\,Mpc^{-1}}$, $\Omega_M = 0.3$, and $\Omega_\Lambda = 0.7$ to allow for ease of comparison with other observational studies. All magnitudes listed follow the AB magnitude system (J. B. Oke 1974; J. B. Oke & J. E. Gunn 1983).

2. Data Reduction and Products

2.1. Surveys and Fields

The data we use for this analysis originates from the Early Release Observations (ERO) and GTO public data taken in Cycle 1, including: CEERS, JADES, GLASS, and SMACS 0723, alongside the PEARLS GTO Survey fields: El Gordo, Clio, MACS-0416, and the North Ecliptic Pole (NEP; R. A. Windhorst et al. 2022) as well as the data from the NGDEEP survey. The data we use are mostly from observations taken with the Near Infrared Camera (NIRCam; M. Rieke et al. 2005; M. J. Rieke et al. 2008; G. H. Rieke et al. 2015) of these various fields and pointings. A list of our fields and their properties is shown in detail in Table 1. We generate data sets for each of these fields, which are reduced in a homogeneous way, and we catalog them in the same way for each field. We do this by consistently processing our data ourselves at all steps using a bespoke and refined method that maximizes our detections of faint galaxies, and the accuracy with which we can measure their photometry.

We call this collation of data the EPOCHS sample, and this paper is the introductory version of this series with succeeding papers describing various aspects of these galaxies and what they imply for galaxy evolution and formation. The sample we describe here is the version 1 (v1) of the EPOCHS sample, while future studies will use different selections and increase our data using more JWST imaging and spectroscopy.

We list in Table 1 the different fields in which this study and the other studies from EPOCHS are taken. We calculate depths for these fields by placing non-overlapping apertures in empty regions of each of the images using `SExtractor` segmentation maps and our image masks. We then used 200 apertures to calculate the normalized mean absolute deviation (NMAD) of these measures to derive local depths for each individual source.

The public data we use includes the CEERS, NGDEEP, JADES, GLASS, and SMACS surveys and fields that have been discussed in previous papers (e.g., T. Treu et al. 2022; S. L. Finkelstein et al. 2023). However, this is not the case for the PEARLS data sets, which make up a large fraction of our sample of high-redshift galaxies. As can be seen in Table 1, the PEARLS area constitutes about 38% of the total area in which we take our survey data on distant galaxies from.

Observations of the three PEARLS lensing fields of SMACS 0723, MACS-0416, and El Gordo, are such that one of the two

NIRCam modules in each pointing is positioned such that it is centered on the lensing cluster. The other module is located approximately 3′ to the side, giving effectively a "blank-field" view of the distant Universe. Although we reduce both modules in these fields, we decided not to include sources found in the cluster module in this study. The high-redshift galaxies directly behind these clusters will be presented and discussed in a future study, using methods similar to the ones used in this paper. By not including the cluster region in our analysis, we simplify things such that we do not need to consider strong gravitational lensing and contamination from intracluster light, which are significant effects (e.g., A. Griffiths et al. 2018; R. Bhatawdekar & C. J. Conselice 2021). For these clusters, only the NIRCam module that is not centered on the cluster is used in our analysis, and thus high-z galaxies lensed behind magnifying clusters of galaxies are not included in this analysis.

2.1.1. PEARLS Fields and Data

The prime fields from which the EPOCHS sample is taken include the Prime Extragalactic Areas for Reionization Science GTO Survey (PEARLS; PI: R. Windhorst & H. Hammel, PID: 1176 & 2738). PEARLS is unique among the early GTO programs in that it is concentrated on imaging new deep fields, including the NEP region, as well as examining distant galaxy clusters. Several of our PEARLS fields are observed with a cadence that allows for variability to be detected (H. Yan et al. 2023). This includes the discovery of one of the highest-redshift supernova discovered to date (B. L. Frye et al. 2024). A full and complete overview of the PEARLS survey can be found in R. A. Windhorst et al. (2022).

As of writing, PEARLS has completed four series of observations. Four of these include targets in and around gravitationally lensing galaxy clusters and one within a blank field. The three clusters we include in this paper are MACS 0416, Clio, and El Gordo. The blank field is located at the NEP. While most of this data has priority time, the first two NIRCam pointings of the NEP were made publicly available. The majority of PEARLS observations we consider within this paper consist of eight NIRCam photometric bands: F090W, F115W, F150W, F200W, F277W, F356W, F410M, and F444W. However, observations of the Clio cluster, a compact lensing cluster at $z = 0.42$, do not include F115W or F410M (A. Griffiths et al. 2018). A typical distribution of depth versus area in the Pearls fields is shown in Figure 1 for the NEP field.

As described already briefly, for the lensing fields of Clio, SMACS 0723, MACS-0416, and El Gordo, the observations include pointings with one NIRCam module centered on the lensing cluster, with the second module offset around 3 arcminutes in a "blank" region. While we reduce both modules in these fields, we do not include sources found in the module containing the lensing cluster in this study. MACS-0416 was observed across multiple visits for time-domain science at three separate position angles, resulting in three parallel "blank" regions that we incorporate.

Where possible, we incorporate complementary observations from HST, particularly optical observations with the ACS WFC instrument, which covers a wavelength range below the NIRCam F090W filter and allows for observation of the Lyman-break at $z < 7$. A list of the fields for which we have utilized ACS data is included in Table 1. Specifically, the NEP time-domain field (TDF) was observed with HST ACS/WFC as part of programs GO-15278 (PI: R. Jansen) and GO-16252/16793 (PIs: R. Jansen & N. Grogin) between 2017 October 1 and 2022 October 31. A mosaic of the F606W observation, astrometrically aligned to Gaia/DR3 and resampled on 0.″03 pixels, were made available pre-publication by R. O'Brien et al. (2024).

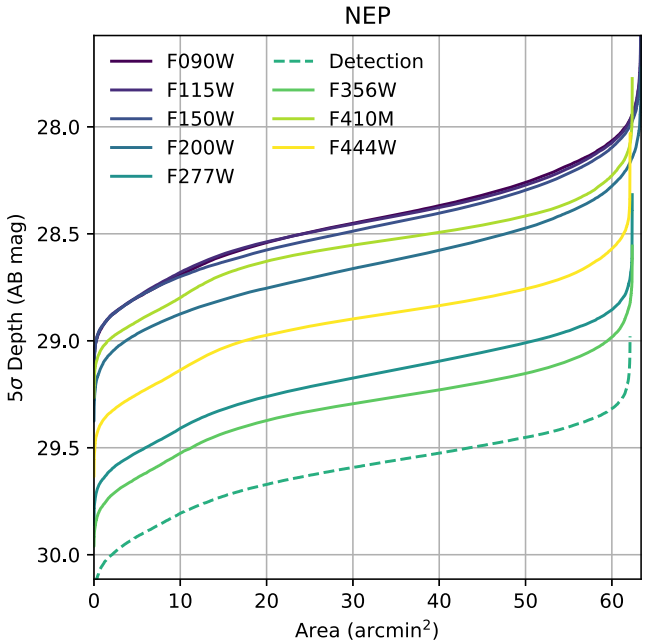

Figure 1. Plot showing the cumulative distribution of unmasked area as a function of depth within the NEP field for the different filters in which this data was obtained. Also shown is the cumulative depth and area for our detection method, which uses an inverse variance weighted stack of the three reddest wideband filters—F277W, F356W, and F444W. This plot gives us an idea of the different depths reached and in which filter over the area of the NEP field. The other EPOCHS fields we use in this paper have similar patterns of depth and area.

2.1.2. SMACS-0723 Field and Data

The first JWST data and imaging publicly released in 2022 July was the SMACS-0723 field, which contains a galaxy cluster, as well as a parallel blank module. Our early analysis of this field was presented in N. J. Adams et al. (2023) with further details in N. J. Adams et al. (2024). The observations of the SMACS-0723 galaxy cluster were part of the JWST Early Release Observations (ERO) program (PID: 2736, PI: K. Pontoppidan, K. Pontoppidan et al. 2022). This cluster was observed in 6-band NIRCam photometry in the F090W, F150W, F200W, F277W, F356W, and F444W filters. However, SMACS-0723 is missing the critical F115W filter, which makes it difficult to identify galaxies at $8 < z < 10$ with certainty.

Within the EPOCHS sample, we include high-z candidates from SMACS-0723 in our final catalogs, but only with care and attention to which redshifts are being used. For example, we do not use this field when measuring the UV luminosity function (N. J. Adams et al. 2024). In more detail, the absence of the F115W photometric band leads to a very significant scatter in photometric redshift measures for galaxies within the redshift range of $7 < z < 10$. However, higher-redshift objects can be identified confidently (e.g., N. J. Adams et al. 2023). Although, we do know that spectroscopic measurements for this sample prove that some of these galaxies are correctly identified as

high-z sources (J. A. A. Trussler et al. 2022b). Thus, while we can identify high-z galaxies in this field, understanding which redshift bin they are in is more of a challenge for $z < 10$. However, we can still examine these systems and their properties as individual detections at more confident redshifts.

2.1.3. The GLASS Field and Data

The GLASS observation program focuses primarily on the A2744 galaxy cluster with a selection of JWST instrumentation (ID: 1324, PI: T. Treu; T. Treu et al. 2022). In parallel to these observations, the GLASS program has generated one of the deepest NIRCam imaging sets publically available. GLASS contains two overlapping parallel NIRCam observations in seven filters: F090W, F115W, F150W, F200W, F277W, F356W, and F444W. This field has already provided several strongly detected high-redshift candidates up to $z = 12.5$ (e.g., M. Castellano et al. 2022; R. P. Naidu et al. 2022).

2.1.4. The CEERS Field and Data

This study also makes use of both observing runs (2022 July and 2022 December) observed as part of the CEERS survey (ID: 1345, PI: S. Finkelstein; see also M. B. Bagley et al. 2023). This consists of nine NIRCam pointings with seven photometric bands (F115W, F150W, F200W, F277W, F356W, F410M, and F444W). This field subsequently provides the single largest area used in our study at 66.4 square arcminutes. However, the lack of observations in the F090W band limit the capabilities of the JWST observations within this field for identifying galaxies at $6.5 < z < 8.5$, so we incorporate HST ACS WFC F606W and F814W observations taken as part of the CANDELS program (N. A. Grogin et al. 2011; A. M. Koekemoer et al. 2011) and re-released as part of the CEERS teams HDR1 data release.

2.1.5. The NGDEEP Field and Data

This study also makes use of the NGDEEP (ID: 2079, PIs: S. Finkelstein, Papovich, and Pirzkal; M. B. Bagley et al. 2023) reduction and high-z sample that was obtained in the work of D. Austin et al. (2023). The data from this field follows the same reduction and selection procedures used for the other JWST fields we study. NGDEEP consists of NIRCam imaging that was run in parallel to JWST's Near Infrared Imager and Slitless Spectrograph (NIRISS) spectroscopy of the Hubble Ultra Deep Field (HUDF). The NIRCam imaging covers part of the HUDF-Par2 parallel field and consists of six broadband filters: F115W, F150W, F200W, F277W, F356W, and F444W, all with average depths of $m_{\rm AB} > 29.5$. It is subsequently the deepest data set used in this study. For more details, see D. Austin et al. (2023) and M. B. Bagley et al. (2023). In addition to the JWST data we use for the NGDEEP field, we also include HST imaging in the F606W and F814W bands from v2.5 of the Hubble Legacy Fields project (G. Illingworth et al. 2016; K. E. Whitaker et al. 2019). In fact, we find that when we include this imaging in the fits, we find that several galaxies are no longer identified as being high-z when using just the JWST bands (D. Austin et al. 2023). This is critical for our analysis and demonstrates the importance of using HST data when possible for exploring distant galaxies with JWST.

2.1.6. The JADES GTO Data

In 2023 June, the JWST Advanced Deep Extragalactic Survey (JADES; PID:1180, PI: D. Eisenstein; A. J. Bunker et al. 2023; D. J. Eisenstein et al. 2023; K. N. Hainline et al. 2024a) team kindly released part of their data products, including the raw imaging, which we use in this paper to find in an independent way, the highest-redshift sources. This data was released in 2023 June, including full mosaics using the pmap1084 (H. Bushouse et al. 2022) calibrations (M. J. Rieke et al. 2023). This released data consists of six overlapping NIRCam pointings from the JADES DEEP observations within the filters: F090W, F115W, F150W, F200W, F277W, F335M, F356W, F410M, and F444W. This field is located around the HUDF in the GOODS-S area. As can be seen in Table 1, the depth of the JADES data within the JWST bands ranges from 29.58–30.21 in its deepest band in F277W. This field also has deep F606W data from ACS.

For the EPOCHS analyses, we rereduce this NIRCam data using our own version of the pipeline for consistency with our other fields. Our bespoke reductions have depths that are around 0.1 magnitude shallower than the official JADES reductions, with one small region of the field affected by residual wisping in the F150W and F200W bands. We also use the same HST/ACS F606W mosaic of the wider GOODS-S region as we use for the analysis of the NGDEEP field.

2.2. Reduction Process

We reprocess all of our uncalibrated lower-level JWST data products and data using the methods outlined in L. Ferreira et al. (2022) and N. J. Adams et al. (2024). This includes reprocessing all of the NIRCam imaging from their lowest-level, raw form obtained from the MAST database using computers at the University of Manchester. We follow the same procedures as used in these published works, but include a series of minor improvements, which we developed over the first year of handling JWST data involving innumerable experiments and trials of different reduction processes.

Below we give a description of the pipeline and processes used to arrive at our final reduced imaging data. Our full pipeline can be summarized through the following steps. First, we use version 1.8.2 of the official JWST pipeline and CRDS v1084 for the calibration files, which contains the most up-to-date NIRCam calibrations at the time of writing. These files also include the third round of post-flight calibrations, which are essential for achieving a reliable photometric calibration and flat-fielding, an issue that has plagued the early analysis of JWST distant galaxy discoveries (N. J. Adams et al. 2023; J. Rigby et al. 2022). After running "Stage 1" of the JWST pipeline, we subtract off templates of 'wisps'. These are large-scale artifacts in the imaging caused by rogue light, and these features affect the A3, A4, B3, and B4 NIRCam modules for the F150W and F200W imaging. The templates we use are the second-generation templates released by STScI.[23] This method has been effective for most observing programs, which we utilize; however, the ultra-deep and small dithering nature of the NGDEEP observations result in some residual wisps that affect the final depths achieved in these two blue filters (e.g., D. Austin et al. 2023). We are presently developing a new series of improved wisp templates to solve these minor issues

[23] https://jwst-docs.stsci.edu/jwst-near-infrared-camera/nircam-instrument-features-and-caveats/nircam-claws-and-wisps

(Adams et al. 2025, in preparation), which will be implemented in v2 of the EPOCHS data set.

Next, our data goes through "Stage 2" of the pipeline, and we apply a $1/f$ noise correction derived and provided by Chris Willott.[24] We then extract the sky subtraction step from "Stage 3" of the pipeline and run this independently first on each NIRCam frame. This allows for a rapid assessment of the background subtraction performance from which we fine-tune our process. We do this by conducting an initial flat background subtraction, which is then followed by a two-dimensional background subtraction utilizing the tool `photutils` (L. Bradley et al. 2022).

The "Stage 3" process is then run on these background-corrected frames, and a final mosaic is produced such that we align the WCS of GAIA DR3 (e.g., Gaia Collaboration et al. 2022) using `tweakreg`, part of the DrizzlePac python package. We then ensure that all of our final images are aligned with one other by aligning them to the F444W image.[25] From this, we pixel-match the images to match the F444W image using the method from `reproject`[26] with the final scale of the drizzled images at $0.''03$ pixel^{-1}.

Our reductions of all of the frames and images in each field differ from the official PEARLS and public team reductions described in papers such as R. A. Windhorst et al. (2022). However, we carry out our reductions in a systematic way across all of our fields, to avoid problems with inhomogenous data quality, methodology, and systematics that can be present when comparing data in different fields reduced in different ways. These issues can be seen from ground-bases surveys as well as in space-based data (e.g., C. J. Conselice et al. 2022). A further description of our reduction and pipeline process is provided in N. J. Adams et al. (2024) and T. Harvey et al. (2024).

2.3. A Robust Sample of Ultra-high-redshift Sources

This Section describes how we identity our high-redshift galaxy candidates, which we later use to determine the properties of early galaxies, as well as for the sample that is used in other papers in this series to investigate the mass function (T. Harvey et al. 2024), the UV luminosity function (N. J. Adams et al. 2024), as well as properties such as galaxy structure, AGNs, star formation, and dust content, which are present in various degrees within our galaxy sample (e.g., I. Juodžbalis et al. 2023; K. L. K. Fu et al. 2024).

In this Section, we first describe how we measure the photometric redshifts for our sample and then we describe how we use this information combined with the detection significance of our sample to create a high-quality sample of $z > 6.5$ candidates for our detailed studies.

2.3.1. Photometry and Detection

To construct our catalogs of objects after our reduction procedure, we utlize the software package `SExtractor` (E. Bertin & S. Arnouts 1996). Our analysis with source extraction runs in dual-image mode, using an inverse variance weighted stack of the F277W, F356W, and F444W bands and by performing forced aperture photometry for multiband measurements.

We calculate photometry for each galaxy within circular apertures of $0.''32$ diameter, including an aperture correction derived from simulated `WebbPSF` point-spread functions (PSFs) for each band used (M. D. Perrin et al. 2012, 2014). We chose this diameter to enclose the central and brightest 70%–80% of a point source's flux, but which is still small enough to avoid contamination. By doing so, we balance the use of high-signal pixels when computing fluxes, and avoid dependence on a PSF model correction that is as high or higher than the measurement made. We found from experimentation that this is the best method for measuring the fluxes of our objects, which obtains most of the light from galaxies without significant contamination from other sources.

To determine the depth of our final images, we use circular apertures in regions of the image where no pre-existing sources are known to exist and which are not within $1''$ of the aperture's central coordinate. This allows us to derive an average depth for each field, as well as to calculate local depths across each field. In order to generate more realistic photometric errors, we calculate the final errors for each source using the NMAD of the nearest 200 empty apertures (D. C. Hoaglin et al. 1983). This process is necessary, as `SExtractor` is known to underestimate photometric errors, and these errors are critical for deriving the photometric redshifts and other galaxy properties accurately. The average depths of each photometric band for each field are presented in N. J. Adams et al. (2024), in the context of using this data to measure the UV luminosity function.

For each of our fields, we also carefully examine and mask out within the image "defect areas" such as diffraction spikes, remaining snowballs, and any high-intensity intracluster medium, which for our objects is very rare. We do this within the NIRCam modules that include foreground clusters, as well as a buffer area around the edges of the images. We find that the edges of the images may be shallower due to the dithering patterns used in the JWST observations. This study only utilizes the total unmasked area, including the low signal-to-noise edges, which are also masked, which is listed alongside the average depths of each field in N. J. Adams et al. (2024), T. Harvey et al. (2024), and Table 1. This process also ensures that we do not include galaxies whose features, in particular bands, are influenced by noise properties.

2.3.2. Photometric Redshifts

With the imaging and cataloging complete, we calculate the NIRCam derived SEDs for all sources identified in order to derive photometric redshifts. We also include a detailed discussion of photometric redshifts for this sample in other papers such as N. J. Adams et al. (2024), T. Harvey et al. (2024), and Q. Duan et al. (2024a). We give another description here that is focused on our particular sample of galaxies used within this paper.

To measure photometric redshifts, we utilize the `EAZY` photometric redshift code (G. B. Brammer et al. 2008) with the default pipeline set to "tweak_fsps_qsf_v12_v3," which were generated using C. Conroy & J. E. Gunn (2010) models. We also incorporate Set 1 and Set 4 of the templates presented in R. L. Larson et al. (2022), which provides bluer rest-frame colors and high equivalent-width emission lines, due to their young ages (between 10^6 and 10^7 yr). These templates have been found to better reproduce the observed colors of some high-z galaxies at redshifts greater than $z = 8$. These additional

[24] https://github.com/chriswillott/jwst
[25] https://github.com/spacetelescope/drizzlepac
[26] https://reproject.readthedocs.io/en/stable/

templates, and our use of emission lines, also allow us to remove the contamination of confusing lower-redshift galaxies at high redshift, as seen in early JWST results (e.g., P. Arrabal Haro et al. 2023a). The redshift range allowed in our study is $0 < z < 25$, and we take the maximum likelihood draw ($z_{\rm ml}$) of the redshift PDF distribution as our redshift estimate, although we note that in the vast majority of cases, this is very close to or the same as the median of the PDF. We do not incorporate any optional prior on apparent magnitude.

We have refrained from employing techniques for fine-tuning the zero-points of the photometric bands in EAZY, as the NIRCam modules consist of multiple individual chips (eight in the blue and two in the red), each with their own independent calibrations and photometric zero-point offsets. Applying zero-point modifications on a chip-by-chip basis, instead of on the final mosaic, would be necessary due to the small field of view covered by each chip, which results in a limited number of objects with spectroscopic redshifts within each chip. This approach could easily introduce potential bias toward certain galaxy colors, depending on the types of spectroscopically confirmed galaxies within each module. These photometric band offsets are however used by others to optimize their photometric redshifts for high-z JWST galaxies (e.g,. K. N. Hainline et al. 2024b; J. R. Weaver et al. 2024a).

Discussions with members of the community have indicated that residual zero-point errors are anticipated to be around 5%. Therefore, we have implemented a minimum 10% error on the measured photometry to account for potential zero-point issues within the NIRCam reduction pipeline in addition to other error sources, such as minor imperfections in the template sets or PSF corrections.

We identify our sample using the fact that distant galaxies at $z > 6.5$ have very distinctive spectral features in the rest-frame UV. This includes the fact that the spectrum bluer than the Lyman-limit at 1216 Å is more-or-less absent due to the absorption of the light from neutral hydrogen gas. These features can produce galaxies seen as drop-outs, and this has been a traditional way to find the most distant galaxies for over 30 yr (e.g., C. C. Steidel & D. Hamilton 1992). Despite this, these apparent "drop-outs" can result from the Balmer break, dust absorption, and nebular lines in lower–z systems. Thus far, few of the highest-redshift galaxies observed with NIRSpec have detected emission lines at $z > 10$, and thus, our redshifts for the highest-redshift galaxies will mostly be based on the continuum shape and the Lyman-break presence versus Balmer break (e.g., Figure 4 of E. Curtis-Lake et al. 2022; S. Fujimoto et al. 2023; S. Carniani et al. 2024).

Overall, we can quantify the photometric redshift quality in a few ways. One of these is to measure the difference between the photometric and spectroscopic redshifts. For our sample, we show this comparison in Figure 2. Figure 2 demonstrates the agreement between our photometric redshifts and the spectroscopic redshifts from sources described below. We can further quantify the quality of our photometric redshifts by the value of the NMAD for the photometric redshift difference with the spectroscopic data. This quantity is defined by:

$$\sigma_{\rm NMAD} = 1.48 \times \ {\rm median}\left(\frac{|\Delta z|}{1 + z_{\rm spec}}\right), \qquad (1)$$

such that $\Delta z = z_{\rm phot} - z_{\rm spec}$ is the difference between photometric redshifts and spectroscopic redshift. Note that the normalizing factor of 1.48 in the $\sigma_{\rm NMAD}$ equation is such that the NMAD expectation value is equivalent to the standard deviation of a normal distribution. We carry out this comparison by using spectroscopic redshifts for galaxies within our EPOCHS v1 sample. At the time of writing this paper, there were a few published spectroscopic redshifts within our fields. This includes those from: the JADES DR3 (F. D'Eugenio et al. 2025) release, a compilation of spectra and redshifts from the Extended Groth Strip (EGS) region from CEERS (P. Arrabal Haro et al. 2023b), including a follow-up DDT program (PID 2750 P. Arrabal Haro et al. 2023a) and PID 2565 (K. Glazebrook et al. 2024). We also include spectroscopic redshifts for the GLASS-z12 object (M. Castellano et al. 2024), including recent results from the MACS-0416 field (Z. Ma et al. 2024) and the SMACS-0723 ERO program (K. Pontoppidan et al. 2022).

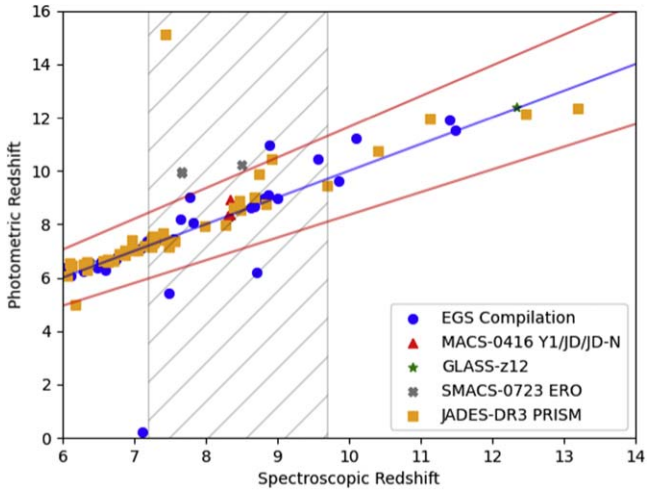

Figure 2. A comparison between the photometric and spectroscopic redshifts for our sample, where available. We compare against recent results from JADES DR3 (F. D'Eugenio et al. 2025) and a compilation of spectra from the EGS region featuring data from CEERS (P. Arrabal Haro et al. 2023b), the follow-up DDT program (PID 2750; P. Arrabal Haro et al. 2023a), and PID 2565 (K. Glazebrook et al. 2024). Also added are spectroscopic redshifts for GLASS-z12 (M. Castellano et al. 2024), recent results from the MACS-0416 field (Z. Ma et al. 2024), and the SMACS-0723 ERO program (K. Pontoppidan et al. 2022). The gray hatched region indicates the region where the lack of F115W in SMACS-0723 leads to larger expected uncertainties. Samples have been cut to show those that are 5σ detected, unmasked, and have strong spectroscopic flags. This shows the quality of our results and methods in finding secure and robust redshifts.

Using these spectroscopic redshifts and those that we calculate with the photometric redshifts, we find that the NMAD values are 0.021 for redshifts $z > 6.5$, which are all within our redshift range. In terms of the outlier fraction, defined as those with a dz $> 15\%$, we find that nine out of 86 objects have redshifts with differences this high at $z > 6.5$. When we omit the cluster SMACS-0723 (due to lack of the F115W making some redshifts quite uncertain at $7.5 < z < 9.5$), the fraction of outliers is then about $\sim$7% (6/83). The result is a photometric redshift sample of high quality determined by this comparison with galaxies with confirmed spectroscopic redshifts.

2.3.3. The Final EPOCHS Sample

To select a robust sample of high-redshift galaxies, we employ a series of selection criteria that we outline below; although, see N. J. Adams et al. (2024) and T. Harvey et al.

(2024) for a further description of this process. The list of criteria and the process for finding these galaxies is given below.

Using the photometric redshift results, we know the location of the likely Lyman-break for each galaxy, which is then used as the pivot point to test whether the data is detected at enough significance for us to include in our sample. The process for doing this is described below:

1. To be included in our sample, the galaxy must be detected at $>5\sigma$ significance in the two bands immediately redward of the estimated Lyman-break position based on the photometric redshift with EAZY, and with nondetections, or less than 3σ detections, in all bands (minimum of a single band) blueward of the Lyman-break. This is to ensure that our galaxies are well detected in the redder bands, and are not detected below the inferred Lyman-break and to remove all obvious Balmer break sources at lower redshifts. If the candidate is a F200W dropout, we increase this to a 7σ and 5σ requirement in the first two bands redward of the Lyman break, as we have observed a number of spurious sources (similar to the $z \approx 16$ candidate in C. T. Donnan et al. (2023), which appeared only in the long wavelength observations, but was later found, via spectroscopy, to be a $z = 5$ interloper (P. Arrabal Haro et al. 2023a).
2. We use the integrated probability density function of our photometric redshifts, PDF(z), to determine the likelihood of the galaxy being at a particular redshift. We require that the integration of the PDF within the range of 10% of the peak photometric redshift PDF value must include at least 60% of the total PDF integral. We do this to remove galaxies that have strong bimodal solutions, particularly where one solution is at low redshift. Other descriptions of this method used for finding galaxies in pairs and in groups can be found in C. J. Mundy et al. (2017), K. Duncan et al. (2019), and F. Sarron & C. J. Conselice (2021).
3. For each galaxy, we perform an additional fit with EAZY runs with a maximum redshift of $z = 6$ allowed in the fits. This allows us to obtain the best "low-redshift" solution for each galaxy. We require that the difference in the χ^2 between the high-z and low-z solutions be $\leqslant -4$.
4. From the samples that pass the above tests, we define a "robust" sample and a "good" sample depending on the quality of the fit. We define the "robust" sample as those galaxies with redshift fits with $\chi^2_{\rm red} < 3$ and "good" as those with a fit giving $\chi^2_{\rm red} < 6$. We do not distinguish between these two sets further in this paper, and both are included in our EPOCHS v1 sample.
5. We compare the candidate's half-light radii to model PSFs as a way to remove likely hot pixels. Objects with sizes significantly smaller than a PSF (half-light radius <1.5 pix.) in the long wavelength detectors are removed as likely artifacts. Note that we do not remove objects that are only close to the size of the PSF without other criteria not being met.
6. To ensure the quality and reliability of the sample, all objects are subjected to visual inspection by multiple authors to identify and remove any artifacts or contaminated sources. This meticulous vetting process involves careful examination of each object's characteristics, such as its morphology, brightness, and consistency with expected high-redshift galaxy features. Any objects that are deemed as artifacts or contamination are removed from the final sample to ensure the integrity of the results. This process ensures that only genuine high-redshift galaxies are included in the final sample. We have endeavored to implement as many of our selection cuts as specific criteria in order to increase the reproducibility and fidelity of our sample. We remove $\leqslant 10\%$ of our total sample by eye, which is significantly lower than some comparable studies.

In Table 2 we list the properties of our sample which we include in our catalog of the EPOCHS v1 galaxies, which are themselves listed individually in Table 3. This catalog in Table 3 are those systems which have passed all of our criteria, whose properties include the redshfits and absolute magnitudes of each system as listed in Table 2.

In N. J. Adams et al. (2024), we included a discussion of how well our results compare with previous studies in the context of using these results for deriving properties of galaxies, including the UV luminosity function. However, that paper did not include an analysis of all galaxy detections, as it only carried out corrections for the luminosity function for galaxy bins in UV luminosity that were more than 50% complete. This means that many of the fainter and lower-mass systems would not have been included in that analysis. As opposed to this, we include and analyze all significantly detected galaxies that pass our criteria within this paper.

2.4. Galaxy Properties from Bayesian SED Fitting

We measure galaxy physical properties using the Bayesian SED-fitting code Bagpipes (A. C. Carnall et al. 2018; A. Carnall 2019). Bagpipes allows flexibility in the choice of models, priors, and SFHs, which can have a large impact on derived galaxy properties (e.g., A. Carnall 2019; C. Pacifici et al. 2023). A complete analysis of the range of physical parameters derived for our galaxy sample given different SED-fitting tools, SFHs, and priors are published and discussed in great detail in EPOCHS IV (T. Harvey et al. 2024).

While we have many different possible stellar masses to use, computed through different parametric and nonparametric methods, in this paper we present results of our fiducial Bagpipes run. These runs are based on a log-normal SFH with logarithmic priors on age, dust extinction, and metallicity. The log-normal SFH was chosen to represent the predicted 'rising' star formation rate of high-z galaxies (e.g., P. Madau & M. Dickinson 2014). Dust, metallicity, and age in particular are difficult to constrain based on photometry alone, and this choice of prior favors low ages, low dust extinction, and low metallicity, which is predicted by simulations and confirmed by spectroscopy (CITE). We assume D. Calzetti et al. (2000) dust emission, P. Madau (1995) ISM extinction, and G. Bruzual & S. Charlot (2003) stellar population models. We use an informative redshift prior based on our EAZY results, with a Gaussian centered on the median of the EAZY redshift posterior, and the standard deviation based on the average of the 16th and 84th percentiles of the PDF, and capped at $\pm 3\sigma$. These properties are included in our catalog of objects in Table 3.

Table 2
Column Names, Units, and Descriptions for the EPOCHS v1 Catalog, Including Column Names, Units, Descriptions, and Column Shape

Column Name	Unit	Description
		IDs, Positions, Fluxes, and Local Depths
ID		Unique catalog ID, consisting of number and fieldname
ALPHA_J2000	degree	R.A.
DELTA_J2000	degree	decl.
FIELDNAME		Field/pointing the galaxy is in
FLUX_APER_BAND	nJy	Aperture corrected flux in 0.″16 radius apertures
FLUXERR_APER_BAND	nJy	Local depth derived flux error from NMAD of 200 nearby empty apertures
sigma_BAND		Signal-to-noise ratio of detection in 0.″16 aperture
local_depth_BAND	AB Mag	5σ local depth from NMAD of flux in 200 nearby empty apertures
unmasked_BAND	Boolean	Whether galaxy is masked in BAND or not
auto_corr_factor_BAND		Correction factor in BAND for flux outside 0.″16 aperture
		Photometric Redshifts and Selection
zbest		Photometric redshift using EAZY
zbest_l1		-1σ photometric redshift uncertainty using EAZY
zbest_u1		$+1\sigma$ photometric redshift uncertainty using EAZY
chi2_best		χ^2 of EAZY fit
PDF_integral_eazy		$\int_{0.94\times\mathrm{zbest}}^{1.06\times\mathrm{zbest}}$ PDF$(z)dz$ - Integral of EAZY posterior redshift PDF
zbest_lowz		Photometric redshift using EAZY, with $z_{\max} = 6$
chi2_best_lowz		χ^2 of EAZY fit, with $z_{\max} = 6$
		UV Properties
M_UV*	AB Mag	Absolute UV mag in 100Å tophat at 1500Å rest-frame flux at redshift zbest
M_UV_u1	AB Mag	
M_UV_l1	AB Mag	
BETA_UV		UV slope $f \propto \lambda^{\beta}$ (see D. Austin et al. 2024).
BETA_UV_l1		
BETA_UV_u1		
SFR_UV*	$M_\odot$ yr^{-1}	
SFR_UV_l1	$M_\odot$ yr^{-1}	
SFR_UV_u1	$M_\odot$ yr^{-1}	
		Sample Identifiers
certain_by_eye	Boolean	Visual inspection of cutout and SED Boolean
EPOCHS_II	Boolean	Used in EPOCHS II (UV LF)
EPOCHS_III	Boolean	Used in EPOCHS III (UV β and dust)
EPOCHS_IV	Boolean	Used in EPOCHS IV (SMF)

Note. An "*" indicates that the column has been corrected for any flux associated with the galaxy that falls outside the extraction aperture. A full description of the catalog is provided at: https://github.com/tHarvey303/EpochsI.

(This table is available in its entirety in machine-readable form in the online article.)

Table 3
Table of Objects in the EPOCHS v1 Sample Discussed in This Paper.

Name	R.A. deg.	Decl. deg.	f_{F444W} nJy	f_{F277W} nJy	z_{EAZY}	$z_{Bagpipes}$	Stellar Mass $\log_{10}(M_\star/M_\odot)$	SFR_{100} $M_\odot$ yr^{-1}	⋯ ⋯
3652_JADES-Deep-GS+	53.18209	−27.81816	30.80 ± 3.08	27.31 ± 2.73	$6.50^{+0.04}_{-0.09}$	$6.45^{+0.07}_{-0.08}$	$7.6^{+0.1}_{-0.1}$	$0.5^{+0.1}_{-0.1}$	⋯
3285_CEERSP3*+	214.83849	52.88520	331.84 ± 33.18	144.53 ± 14.45	$6.50^{+0.07}_{-0.35}$	$6.65^{+0.08}_{-0.34}$	$10.2^{+0.2}_{-0.3}$	$239.4^{+21.5}_{-24.8}$	⋯
13266_NEP-1	260.76351	65.78839	24.06 ± 2.41	22.95 ± 2.29	$6.50^{+0.06}_{-0.21}$	$6.52^{+0.08}_{-0.12}$	$8.1^{+0.3}_{-0.3}$	$1.0^{+0.2}_{-0.3}$	⋯
4168_CEERSP4+	214.79533	52.79046	18.89 ± 2.02	18.78 ± 1.88	$6.50^{+0.04}_{-0.20}$	$6.39^{+0.11}_{-0.12}$	$7.2^{+0.1}_{-0.0}$	$0.2^{+0.0}_{-0.0}$	⋯
23488_JADES-Deep-GS+	53.16618	−27.76435	7.91 ± 0.79	8.24 ± 0.82	$6.50^{+0.04}_{-0.14}$	$6.47^{+0.09}_{-0.11}$	$6.9^{+0.2}_{-0.1}$	$0.1^{+0.1}_{-0.0}$	⋯
12137_JADES-Deep-GS*	53.18464	−27.77930	10.54 ± 1.05	13.98 ± 1.40	$6.50^{+0.05}_{-0.11}$	$6.50^{+0.07}_{-0.09}$	$7.4^{+0.1}_{-0.1}$	$0.2^{+0.1}_{-0.0}$	⋯
5743_CEERSP10*+	214.83846	52.77877	41.93 ± 4.19	37.40 ± 3.74	$6.50^{+0.05}_{-0.25}$	$6.48^{+0.13}_{-0.19}$	$8.1^{+0.2}_{-0.2}$	$1.7^{+0.7}_{-0.5}$	⋯
4530_CEERSP8	215.05798	52.91688	8.37 ± 2.17	10.79 ± 1.57	$6.50^{+0.04}_{-0.44}$	$6.51^{+0.18}_{-0.27}$	$7.3^{+0.3}_{-0.3}$	$0.2^{+0.2}_{-0.1}$	⋯
16783_NEP-2*	260.76476	65.86070	22.30 ± 2.43	26.46 ± 2.65	$6.51^{+0.04}_{-0.18}$	$6.41^{+0.10}_{-0.11}$	$7.4^{+0.1}_{-0.0}$	$0.2^{+0.0}_{-0.0}$	⋯
15297_JADES-Deep-GS	53.16238	−27.80330	10.81 ± 1.08	8.96 ± 0.90	$6.51^{+0.04}_{-0.28}$	$6.25^{+0.26}_{-0.06}$	$7.4^{+0.2}_{-0.1}$	$0.3^{+0.2}_{-0.1}$	⋯
559_CEERSP3+	214.80648	52.87883	64.48 ± 6.45	64.58 ± 6.46	$6.51^{+0.04}_{-0.30}$	$6.36^{+0.17}_{-0.19}$	$8.1^{+0.1}_{-0.1}$	$1.4^{+0.6}_{-0.4}$	⋯
8857_NEP-1*+	260.74977	65.79742	57.24 ± 5.72	52.02 ± 5.20	$6.51^{+0.04}_{-0.19}$	$6.40^{+0.11}_{-0.13}$	$8.1^{+0.2}_{-0.2}$	$1.5^{+0.7}_{-0.4}$	⋯

Table 3
(Continued)

Name	R.A. deg.	Decl. deg.	f_{F444W} nJy	f_{F277W} nJy	z_{EAZY}	$z_{Bagpipes}$	Stellar Mass $\log_{10}(M_\star/M_\odot)$	SFR_{100} $M_\odot$ yr^{-1}	⋯ ⋯
16342_NEP-3	260.68517	65.93653	69.81 ± 6.98	66.45 ± 6.65	$6.51^{+0.04}_{-0.08}$	$6.47^{+0.06}_{-0.05}$	$7.8^{+0.1}_{-0.0}$	$0.7^{+0.1}_{-0.1}$	⋯
14059_NEP-4*+	260.45029	65.81491	35.99 ± 3.60	42.30 ± 4.23	$6.51^{+0.04}_{-0.28}$	$6.34^{+0.14}_{-0.14}$	$7.9^{+0.2}_{-0.2}$	$0.9^{+0.3}_{-0.2}$	⋯
1167_CEERSP3*	214.82036	52.88475	114.95 ± 11.50	98.59 ± 9.86	$6.51^{+0.05}_{-0.13}$	$6.46^{+0.11}_{-0.11}$	$8.4^{+0.1}_{-0.1}$	$2.5^{+0.7}_{-0.6}$	⋯
36860_JADES-Deep-GS*+	53.10976	−27.80747	188.80 ± 18.88	139.92 ± 13.99	$6.51^{+0.05}_{-0.37}$	$6.03^{+0.05}_{-0.07}$	$9.2^{+0.1}_{-0.1}$	$15.1^{+2.7}_{-3.1}$	⋯
17157_NGDEEP*+	53.26097	−27.82496	11.79 ± 1.18	11.35 ± 1.14	$6.51^{+0.19}_{-0.09}$	$6.52^{+0.09}_{-0.14}$	$7.9^{+0.2}_{-0.2}$	$0.8^{+0.1}_{-0.1}$	⋯
2790_CEERSP8	215.03306	52.89019	27.03 ± 2.70	23.51 ± 2.35	$6.51^{+0.03}_{-0.41}$	$6.25^{+0.21}_{-0.22}$	$8.2^{+0.2}_{-0.3}$	$1.0^{+0.2}_{-0.1}$	⋯
3761_CEERSP9*+	214.91319	52.81510	33.02 ± 3.30	34.81 ± 3.48	$6.51^{+0.04}_{-0.20}$	$6.39^{+0.12}_{-0.13}$	$7.6^{+0.1}_{-0.0}$	$0.4^{+0.1}_{-0.0}$	⋯
12178_NEP-4*+	260.51401	65.81138	91.83 ± 9.18	62.23 ± 6.22	$6.51^{+0.05}_{-0.10}$	$6.44^{+0.10}_{-0.09}$	$8.5^{+0.1}_{-0.1}$	$3.5^{+1.2}_{-0.7}$	⋯
7570_NGDEEP	53.26361	−27.86999	16.18 ± 1.62	17.60 ± 1.76	$6.51^{+0.17}_{-0.14}$	$6.42^{+0.12}_{-0.12}$	$8.4^{+0.1}_{-0.1}$	$0.5^{+0.2}_{-0.1}$	⋯
9077_NEP-2	260.90467	65.82584	27.33 ± 2.73	31.59 ± 3.16	$6.51^{+0.04}_{-0.32}$	$6.30^{+0.17}_{-0.16}$	$7.6^{+0.2}_{-0.1}$	$0.5^{+0.3}_{-0.1}$	⋯
12576_NEP-1*+	260.74459	65.76737	124.25 ± 12.43	112.57 ± 11.26	$6.51^{+0.05}_{-0.09}$	$6.44^{+0.08}_{-0.09}$	$8.5^{+0.1}_{-0.1}$	$3.5^{+0.9}_{-0.6}$	⋯
⋯	⋯	⋯	⋯	⋯	⋯	⋯	⋯	⋯	⋯

Note. The upper-right corner of the full EPOCHS Galaxy Catalogue. A "*" ("+") indicates that the stellar mass (SFR) has been corrected to the full size of the galaxy, based on the fitted `SExtractor` Kron ellipse. This list is a truncated version, with the full catalog available online.

2.5. Brown Dwarfs

Low-mass stars within the Milky Way, particularly L- and T-type brown dwarfs, can masquerade as high-z galaxies due to an apparent Lyman-break like dropout in their broadband SEDs. In order to ensure our sample is not contaminated with brown dwarfs, we fit synthetic brown dwarf templates using a least-squares fitting routine. We use the Sonora Bobcat and Cholla templates (M. S. Marley et al. 2021; T. Karalidi et al. 2021). For each of the SEDs predicted by both sets of Sonora templates, we calculate mock photometric measurements for HST/ACS WFC and JWST/NIRCam filters and fit the model photometry to our observed photometry, varying only the best-fitting normalization.

We flag an object as a possible brown dwarf by comparing the χ^2 values of brown dwarf versus galaxies templates. This is such that an object is identified as a brown dwarf when the $\Delta\chi^2$ between the best-fitting brown dwarf template and the best-fitting `EAZY` galaxy template is <4, which is the same $\Delta\chi^2$ criteria we apply between our low-z and high-z `EAZY` fits. We also additionally require that the galaxy appears compact, as we expect brown dwarfs to appear as point sources, so we require that the 50% encircled flux radius (as measured by `SExtractor`) is smaller than the FWHM of the PSF in the F444W band. In total, across all of the fields, we flag 59 objects as possible brown dwarfs, which is ∼4.6% of the full sample. While the brown dwarf candidates presented in K. N. Hainline et al. (2024b) are not within our initial sample of high-z galaxies, due to not meeting our other criteria, we test our brown dwarf fitting methodology on their candidates and recover and identify all of them as brown dwarfs.

2.6. Galaxy Detection and Completeness

One of our goals within this paper is to have a high degree of completeness and purity within our sample of galaxies. There are various ways to determine this, although understanding this exactly is difficult to impossible without deep spectroscopic studies that are complete to certain magnitude or flux depths. However, one way we can investigate this is to use simulations and mock catalogs of our fields and determine how many distant galaxies within our redshift range of interest we would detect using our methods and criteria for finding distant galaxies.

We compute this using the `JAGUAR` simulation (C. C. Williams et al. 2018). `JAGUAR` is a novel phenomenological model that is designed and meant to describe the evolution of galaxy number counts, morphologies, as well as SEDs across a broad range of redshifts ($0.2 < z < 15$) and at stellar masses log $(M/M_\odot) > 6$. `JAGUAR` essentially creates mock catalogs that reproduce the properties of various deep JWST surveys from which we create mock catalogs for each of our deep fields. It has previously been shown before JWST that the output from `JAGUAR` matches well with observed stellar mass and luminosity functions for both star-forming and quiescent galaxies, and can accurately replicate the redshift evolution of colors, sizes, star formation rates, and chemical properties of the galaxy population. It does this by including a self-consistent treatment of stellar and photoionized gas emission and dust attenuation, utilizing the BEAGLE tool. Thus, the `JAGUAR` simulation produces a list of simulated galaxies, with characteristics such as their redshifts, stellar masses, star formation rates, and other physical properties including the fluxes of each galaxy in each band.

To use `JAGUAR` effectively for a given field, we use the known average depths of each of our fields and apply a Gaussian scatter to each modeled galaxy's photometry accordingly. We thus create a new catalog for the `JAGUAR` sources, such that the photometry is now adjusted to represent how these galaxies would be observed within each different field. This new photometric catalog is then run through our `EAZY` SED fitting and selection procedure. This is done to determine whether, and thus what fraction, of actual galaxies in the `JAGUAR` catalog would still remain detected after going through our selection.

We furthermore apply `Bagpipes` fitting to the simulated data to determine how the stellar masses and star formation rates would have changed due to the limited depth of each field. We thus apply this process to our entire `JAGUAR` catalog, which allows us to determine the fraction of true high-redshift galaxies in our final sample (completeness) and the number of low-redshift interlopers (contamination). These values vary depending on the field, as both the filters and depths differ across fields. We can parameterize the completeness in terms of known variables (stellar mass, M_{UV}, apparent magnitude) by

categorizing the completeness and contamination into bins. A more detailed explanation is outlined in previous EPOCHS papers (T. Harvey et al. 2024; D. Austin et al. 2024), and we describe this further in Appendix A.

3. Results

In this Section, we discuss our sample of high-redshift galaxies and their properties, including their apparent evolution. We first discuss the overall trends of magnitude and luminosity for our sample, and then we explore some of the more detailed properties of our galaxies, including their observed and rest-frame colors, as well as SFHs and how the number of galaxies we find compares with theoretical models as a new test of the excess galaxy problem.

3.1. Redshift Distributions

Figure 3 shows the redshift distribution for our sample, in terms of the observed F444W NIRCam magnitude of each of our sources, as labeled by the field in which they are discovered within. These are "mag-auto" magnitudes as measured by SExtractor. There are a couple of major features that can be seen in Figure 3. The first is that our selection produces galaxies with a relatively high abundance up to $z \sim 12$, but fewer galaxies at higher redshifts. This is likely due to the fact that there are a limited number of galaxies that can be found with JWST imaging at these higher redshifts, as seen in previous work (e.g, N. J. Adams et al. 2023; D. Austin et al. 2023). There are very few bright galaxies in our $z > 6.5$ sample compared to lower-redshift galaxies or those found with HST, and we find that there are galaxies as faint as mag ~ 30 from our deepest pointing in NGDEEP (D. Austin et al. 2023). It also remains to be seen if these $z > 12$ galaxies remain as viable ultra-high-redshift galaxies once NIRSpec data on this sample is obtained.

We can also see that certain surveys favor different redshift ranges. For example, the NEP field is good at finding galaxies at the lower redshift range of our survey, while the CEERS field is superior at finding slightly higher-redshift galaxies. We also find that there are more galaxies per unit area in the NEP field than our other fields. This is due to naturally finding more objects at lower redshifts given the sensitivity of this field to lower redshift, given its filters. This effect however may also be due to a slightly higher contamination due to a lack of depth in some filters or the lack of medium-band filters, such as F335M (e.g., Y. Harikane et al. 2024). This is due to the filter set within each of the observed fields, which differs slightly between the various fields. These different filters probe the SEDs of galaxies in different ways, most notably through the location of the Lyman-break. Some filter combinations make it difficult to find lower-redshift galaxies, as in the case of CEERS due to the absence of the F090W band, as discussed earlier. This limitation gives us a higher certainty on finding more distant galaxies, and less certainty on others, depending on the exact field that is being observed. This also shows the necessity and benefits of combining data from various fields that contain data at not only different areas and depths but different filters, which strongly limits at which redshifts we can find reliable distant galaxy candidates.

Another feature is that the depths of the various data sets differ considerably, and it can be seen that the NGDEEP field finds both the faintest galaxies, both in terms of the F444W

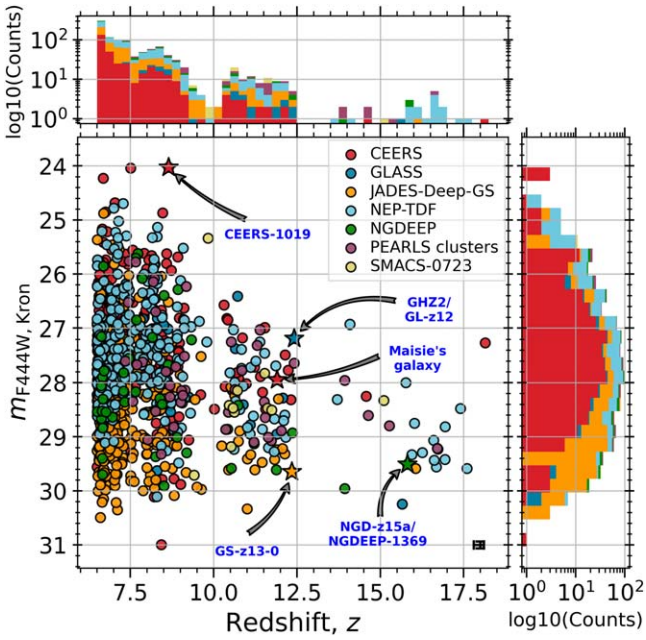

Figure 3. Evolution of SExtractor F444W "MAG_AUTO" apparent magnitudes (measured in Kron apertures; R. G. Kron 1980) with EAZY-py redshifts (z) for our "certain" galaxy sample. The colors indicate the survey of origin, where the purple points in the PEARLS clusters are from the blank parallel fields of the El Gordo, MACS-0416, and Clio clusters. The median 1σ error for the sample is shown in the bottom right. Highlighted are notable spectroscopically confirmed galaxies from JADES (GS-z13-0; E. Curtis-Lake et al. 2022), CEERS (Maisie's galaxy; L. S. Finkelstein et al. 2022), and GLASS (GHZ2/GL-z12; R. P. Naidu et al. 2022; M. Castellano et al. 2022, 2024). The $z = 8.679$ CEERS AGN from R. L. Larson et al. (2023; CEERS-1019), and $z \simeq 15.6$ galaxy candidate from NGDEEP (NGD-z15a/NGDEEP-1369; D. Austin et al. 2023; G. C. K. Leung et al. 2023) are also shown.

magnitude, as well as in absolute UV luminosity as characterized by the values of $M_{\rm UV}$ (Figure 4). Again we can see that the faintest galaxies in the rest-frame UV are found in the NGDEEP field, given its depth and despite its small field of view, relative to the other JWST pointings. We furthermore find several dozen galaxies at the highest redshifts $z > 12.5$ where there are still few to no spectroscopic confirmations. The properties of these galaxies are described later in this paper, but in general these are fairly bright systems, with the exception of a few galaxies found in the NGDEEP field at $z \sim 15$. These are the faintest galaxy candidates known at such low luminosities found at early times.

3.2. Distribution and Evolution of UV Luminosity

We have previously described in detail the UV luminosity function evolution in N. J. Adams et al. (2024), and here we describe other features of our galaxy sample in terms of the distribution and evolution of UV luminosities for individual galaxies. In N. J. Adams et al. (2024), we only include galaxies in the LF calculation if the completeness in any given bin is >50%, and thus, many galaxies in the EPOCHS sample are missing from that analysis. Here we discuss the full range of UV luminosities of our EPOCHS v1 sample.

In Figure 4 we show the distribution of our galaxies in terms of absolute UV magnitude as a function of redshift. As discussed in D. Austin et al. (2024), our $M_{\rm UV}$ calculations are derived directly from the photometry, based on the EAZY photo-z, using the flux between 1450 Å and 1550 Å in the rest frame. Therefore, these measurements are direct, and not based

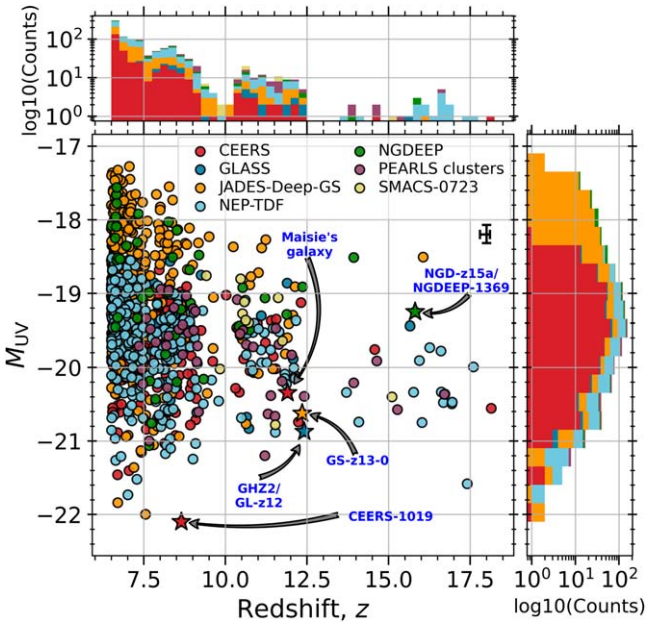

Figure 4. Rest-frame absolute UV magnitudes M_{UV} as a function of EAZY-py redshift, where the colors and highlighted galaxies are shown as in Figure 3. The median 1σ error for the sample is shown in the upper right. We also show the distribution of redshifts as the upper histogram and the distribution of the absolute UV magnitudes in the histogram to the right.

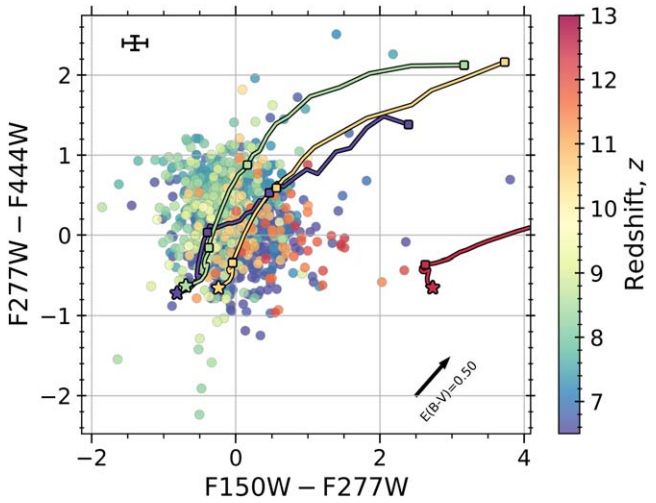

Figure 5. The observed color–color diagram for the galaxies in the EPOCHS sample at $6.5 < z < 13$. We color the points by their EAZY-py redshift, and the median 1σ error for the sample is shown in the upper left. Overplotted are color–color tracks using v2.3 of the Binary Populations and Spectral Synthesis (BPASS; J. J. Eldridge et al. 2017; E. R. Stanway & J. J. Eldridge 2018; C. M. Byrne et al. 2022) SED models at redshifts $z = \{6.5, 8.5, 10.5, 12.5\}$ from roughly left to right, assuming a metallicity $Z = 0.01$, an alpha enhancement of $\Delta \log_{10}(\alpha/\mathrm{Fe}) = +0.6$, and with an initial mass function (IMF) with slope $\Gamma = 1.35$ and a high-mass cutoff of $M_\star = 300 M_\odot$. These models range in age from 1 Myr to 1 Gyr since an initial burst of star formation, with the starred points showing results at 1 Myr and subsequent squares showing colors at $\log_{10}(\mathrm{age/yr}) = \{7, 8, 9\}$. This demonstrates that our sample of galaxies is quite heterogeneous at these early times, and that there is a variety of SFHs present beyond the simple burst we assume here. Since these models do not include attenuation by dust, we additionally show the impact of dust with the arrow in the lower right, assuming a D. Calzetti et al. (2000) attenuation law with $E(B-V) = 0.5$ at $z = 8.5$.

on the SED fits, which the other features of our galaxies are derived from, such as the stellar mass.

This includes the trends and ranges of UV luminosities for our sample. As can be seen, we find that there is a large diversity of galaxy UV brightness consistent with an evolving LF through the first 500 Myr of cosmic time (N. J. Adams et al. 2024). We find very luminous galaxies up to $z \sim 18$, which reveals no obvious observational evolution in the upper limit of UV brightness, which otherwise might decline at higher redshifts. While we do find a gradual trend for galaxies to appear brighter at the highest redshifts, we still find objects with $M_{UV} \sim -18$ at $z \sim 11$, with some candidate systems this faint at even higher redshifts. These correspond to the bluest systems, which we describe later in this paper.

3.3. Color–Color Plots

Another observational clue that we can use to determine the nature of the high-redshift EPOCHS galaxy population is to use color–color diagrams. This provides a purely observational picture of how the SEDs of these galaxies are distributed, which can relate to various features, such as their SFHs, as well as the dust content, and to a lesser degree the metallicities of the underlying stellar populations.

To approach this issue, we use a demonstrative sample of galaxies between $6.5 < z < 13$ and examine a color that, for most galaxies in this range, spans the blue region of the spectrum (F150W–F277W), and the (F277W–F444W) color that probes redder into the SED, covering for most of these redshifts the optical/UV SED. This distribution is shown in Figure 5 with models superimposed. This is a somewhat crude representation of the SEDs of these galaxies, but it still allows us to examine these properties without having to rely on detailed SED fits or other methods that are interpretative. Overall, for the bulk of this sample, the bluer filter color gives us a rest-frame wavelength through the redshift range of $6.5 < z < 13$ of 0.20–0.37 μm to 0.11–0.20 μm. For the longer wavelength color, we are comparing 0.37–0.59 μm up to 0.20–0.31 μm. For most of our redshift range we can consider the (F150W–F277W) color as tracing the UV color which probes younger stars, and (F277W–F444W) as a measure. of the color around the Balmer break, particularly at $z > 8.5$.

Immediately, we can see that the Balmer break colors differ in magnitude spanning $\approx$2 mags for galaxies at $8.5 < z < 10.5$. If this is a relative measurement of age, it implies that our galaxies have a wide diversity of ages, which we later derive through the SED fitting discussed in Section 2.4. The UV color of our galaxies, more representative of recent SFHs, also spans about 2 magnitudes in color, again showing a wide diversity in ages and ongoing star formation rates for our galaxies.

Unlike for the magnitude distribution, we do not, in general, see any bias of the type of galaxies we are obtaining in our different fields, at least in terms of their colors. Thus, while the different JWST bands will allow only certain redshifts to be measured within a given filter set and field combination, this does not create any detailed biases in the underlying types of galaxies that are being retrieved from these fields.

We also overplot on this diagram stellar population models of different ages. This demonstrates in a comparative way that our sample of galaxies has a diversity in SFHs and that galaxies at high redshifts have a range of when their star formation began, and for how long and in what manner the formation histories have been ongoing. In the next Section, we consider these observations in more detail through SED modeling and examining the rest-frame colors of our galaxy sample.

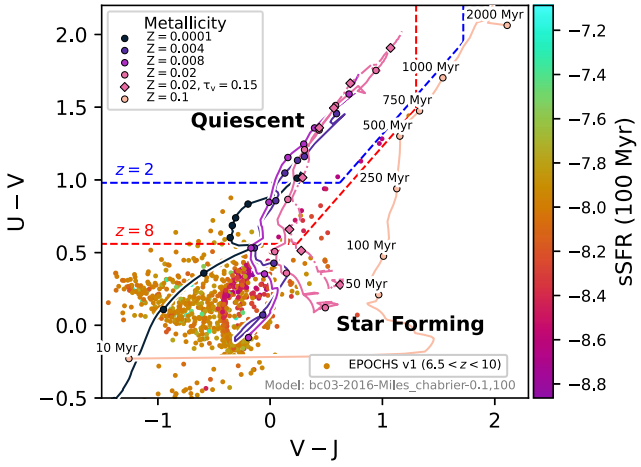

Figure 6. The distribution of our EPOCHS sample at $6.5 < z < 10$ in terms of the UVJ diagram, colored by specific star formation rate (sSFR). As can be seen, we find a range of colors for our sample, yet we find few galaxies that are consistent with being passive, but do find some that are near the passive range. We plot on this Figure modeled evolution of stellar populations within the UVJ plane, showing models of galaxies of different metallcities (Z) within timescales from from 10 Myr to 2 Gyr after a burst of star formation. This version shows G. Bruzual & S. Charlot (2003) stellar population models with 2016 Miles stellar population synthesis models, with a Chabrier initial mass function (IMF). Similar models using BPASS models (J. J. Eldridge et al. 2017) with a Chabrier IMF show comparable trends. For the most part, these models include the intrinsic stellar spectra, with no dust included. The time-markers are (from the bluest, blue point redward) 10, 50, 100, 250, 500, 750, 1000, and 2000 Myr. Also shown are the $z = 2$ and $z = 8$ quiescent defined regions.

Another traditional way to examine this problem is to plot the UVJ diagram for galaxies and to determine where our sample of $z > 6.5$ galaxies is located in this parameter space. We show this UVJ diagram for our sample in Figure 6, with the marker color showing the `Bagpipes` derived specific star formation rate. The majority of our galaxies are in the star formation region of this parameter space, with very few of the systems approaching the area for passive galaxies. However, this is in general what is seen for galaxies at this epoch, in which even galaxies with recently quenched star formation or "smoldering" galaxies are found in the star forming region rather than the passive region of the UVJ parameter space (J. Trussler et al. 2024). It is also the case that galaxies do not enter the passive region of the UVJ region until $z \sim 1.5$. These systems are also mostly compact and elliptical in morphology (C. J. Conselice et al. 2024).

3.4. Rest-frame Color Evolution

While the color–color plots are demonstrative of broad features, they are limited in that they span different rest-frame wavelengths depending on the redshift of the object and are degenerate to some degree between ages, star formation rate, and dust content. To understand these sources better, we carry out detailed SED fitting using the `Bagpipes` code introduced in Section 2.4. Some examples of these fits are shown in Figure 7 for systems that have red colors, while those shown in Figure 8 are examples for blue galaxies. Below these fits, we also show the images of the galaxies as imaged in the different bands in which they are imaged and where the photometry is measured.

Based on these fits, we can retrieve the rest-frame colors of our sample based on the best fits, as shown in the SED Figures. We thus calculate the rest-frame colors of our objects using the best-fitting templates and measure the rest-frame $(U-V)$ colors or these galaxies. This is an indicative color, as it straddles the Balmer break, and thus gives us a good representation concerning how blue or red our galaxies are within this wavelength difference.

We show the rest-frame $(U-V)$ colors of our sample in Figure 9 plotted as a function of redshift. This Figure shows a range of colors at all redshifts, but with a gradual change in average color, such that galaxies at higher redshifts are bluer in their rest-frame $(U-V)$ colors. In addition to this, we also find that there is a collection of galaxies that appear quite blue. We also compare our results in this Figure to the models from the FLARES simulation, demonstrating that there is a relatively good agreement between the data and model. However, our sample is on average slightly redder than the models at progressively lower redshifts, with some very red systems not predicted.

To understand the origin of our sample in more detail, we examine the relationship between the rest-frame $(U-V)$ color and stellar mass in Figure 10. We limit this part of our analysis to galaxies at redshifts $8.5 < z < 10.5$, as this is the redshift range where we have the largest sample of galaxies, as well as being the most reliable in photometric redshifts. When we examine this relationship at this narrow redshift range, we find that there is already present, at such early times, a strong correlation between this color, which straddles the Balmer break at these redshifts, and the stellar mass. This correlation is such that more-massive galaxies are redder in their rest-frame colors. Therefore, what we see is a population of relatively massive red galaxies already established at this early point in the Universe's history. This suggests that galaxy scaling laws are established very rapidly in the universe's history.

This also demonstrates that while there is a diversity of SEDs forms and shapes for the high-redshift sample, there is still a strong trend of color with stellar mass. We discuss the origin of this trend in Section 4, including comparing these data to simulations to understand their nature. This result is however unlikely to be due to selection effects. The reason for this is that we would have easily seen any blue bright massive galaxies at these early types. It is clear that galaxies that are relatively red dominate the massive galaxies sample at $z > 8.5$.

We can also see in the upper-left plot of Figure 10, where the points are colored by redshift, is that there is a redshift evolution within these diagrams. This is such that the higher redshift galaxies form into a bluer sequence of points where mass correlates with color, while the lower-redshift galaxies appear to form a similar slope sequence, but with a redder offset sequence. What remains to be determined from this is how our measurements of color depend on the measurement of the star formation rate for our galaxies, which we examine the next Section.

3.5. The Early Galaxy Main Sequence

Using our data and results, we can probe the formation of the main sequence of galaxies. This main sequence is such that there exists at lower redshifts a well-defined correlation between galaxy stellar mass and star formation rate (e.g., K. G. Noeske et al. 2007; A. E. Bauer et al. 2011; P. Santini et al. 2017; R. Bhatawdekar & C. J. Conselice 2021). This correlation is such that galaxies with a higher stellar mass have

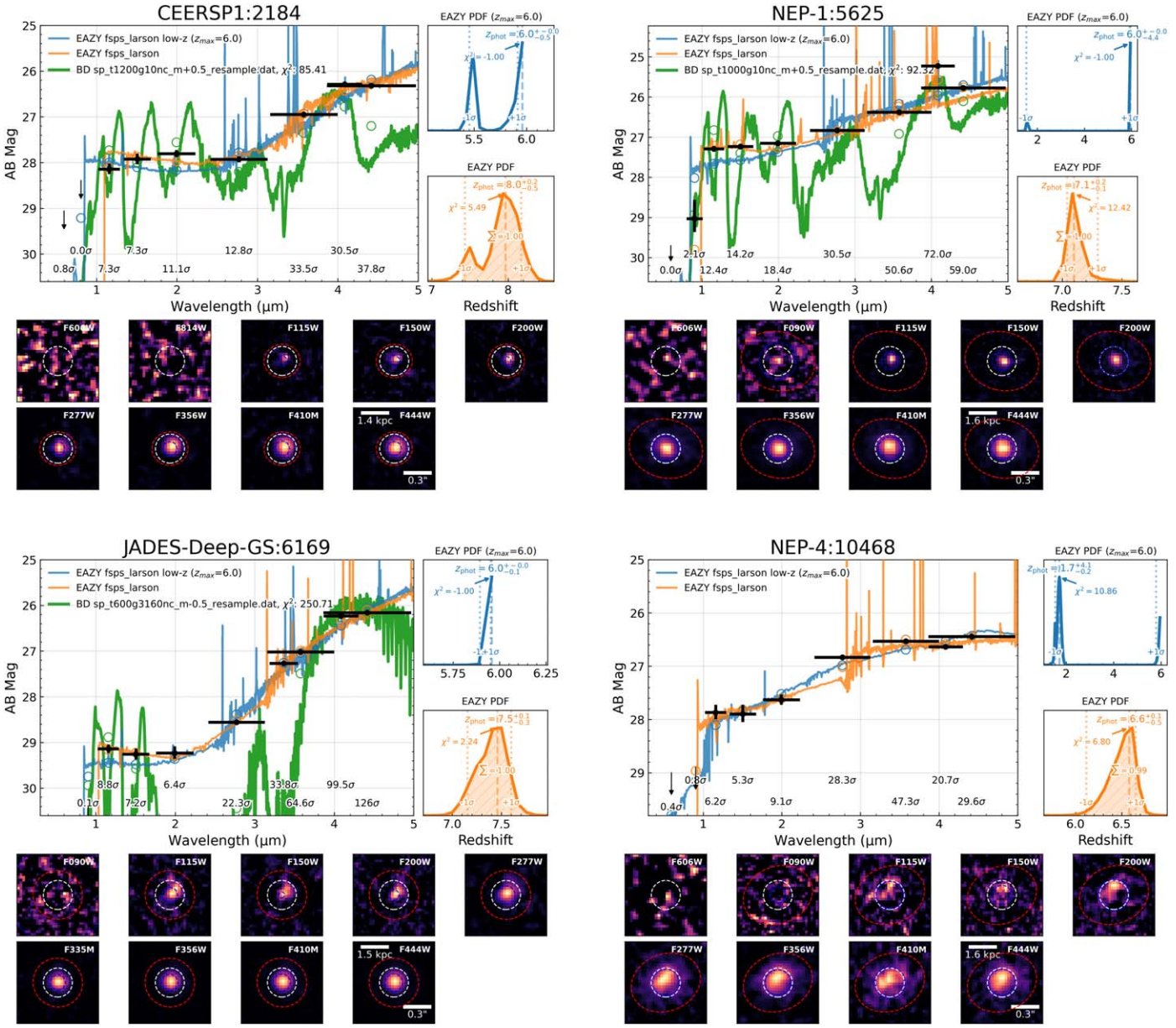

Figure 7. Spectral energy distribution (SED) fits for redder galaxies in our sample. The various panels show the redshift PDFs and photometry for four representative high-z galaxies with red colors for $z > 6.5$ galaxies. These systems are at $z \sim 7$–9 where we have the largest range of galaxy properties given our large sample. The measured photometry for the NIRCam observations are shown in black, with best-fitting EAZY SEDs shown in blue, and in orange for a low-redshift prior at $z < 6$ and a free fit to the redshift, respectively. The green line shows the best fit to templates of brown dwarfs. Overlaid on the redshift PDFs are the selection statistics, including the photometric redshift estimates. The bottom section of panels shows the cutouts of these galaxy candidates in the NIRCam photometric bands, on a log color scale. Note that these galaxies are from different fields that contain different observed bands.

a higher star formation rate, which is independent of how the star formation rate is measured (e.g., K. G. Noeske et al. 2007).

We show the galaxy main sequence for our EPOCHS v1 sample in Figure 11 from our fiducial `Bagpipes` results, on both a 10 Myr and 100 Myr average star formation timescale. We show here the star formation versus stellar mass relation for our galaxies using these two different timescales at 10 Myr (on the right) and over the past 100 Myr (on left). These star formation timescales show the average star formation rate over this time period. One thing to immediately notice is that we see a trend such that, on average, systems with a high stellar mass have a higher star formation rate, and therefore that the main sequence of star formation continues up to the highest redshifts we can measure these up to.

The exact fit of this is difficult to quantify, as the exact value will depend on the form of the assumed SFH in which these star formation measures are taken from. Thus, we demonstrate these plots as a detection of a main sequence, rather than a formal fitting of it. However, we do find that there is very little evolution in the form of the agreement between these two quantities within redshift or within different star formation timescales. It can be seen that even when comparing to previous work at lower redshifts, we do not find a significant amount of evolution in the normalization or the slope of the star formation versus stellar mass relation. We do, however, find some potential differences in previous work measuring this scaling, even within the same redshift range. For example, it appears from Figure 11 that our stellar masses are higher than

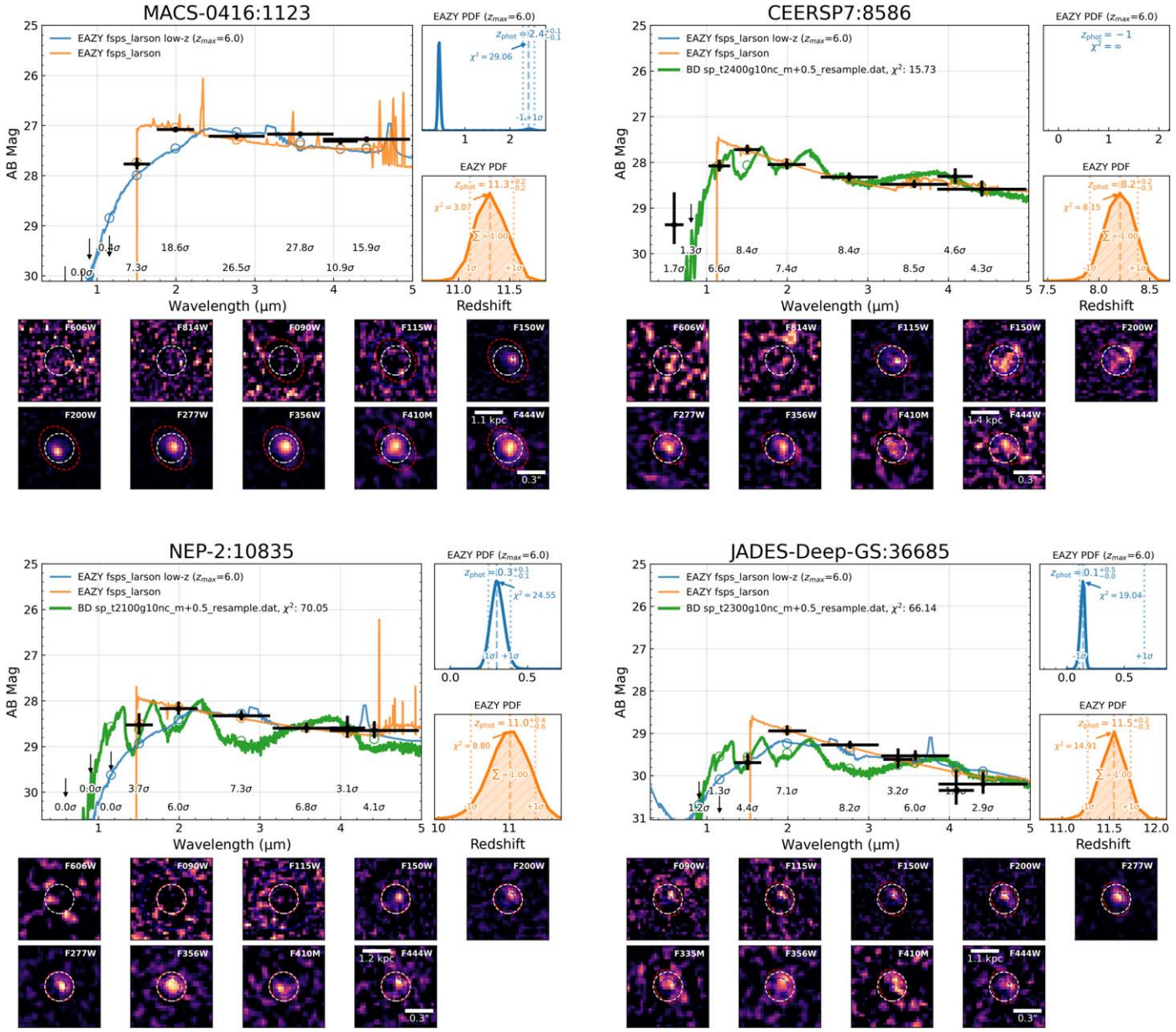

Figure 8. Similar to the previous plots in Figure 7, but for bluer examples in our sample. These panels show the redshift PDFs and photometry for four representative high-z galaxies with blue colors from our $z > 6.5$ sample. The features of the galaxies displayed here are the same as in Figure 7. These blue systems are those found at $z \sim 8$–11, where we have the largest range of galaxy properties within our large sample. The measured photometry for the NIRCam observations is shown in black, with the best-fitting EAZY high-redshift SEDs shown in orange, with the best $z < 6.5$ solution shown in blue. For comparison in green, we also show the best-fitting brown dwarf template, taken from fitting all of the Sonora Bobcat and Cholla synthetic brown dwarf templates. Overlaid on the redshift PDFs are the selection statistics, including the photometric redshift estimates. The bottom section of the panels shows the cutouts of these galaxy candidates in the NIRCam photometric bands, on a log color scale. Note that these galaxies are from different fields that contain different bands for the observations. There are no solutions for the $z < 6$ fits for CEERSP7:8586, which is shown as $z_{\rm phot} = -1$.

those from R. Bhatawdekar & C. J. Conselice (2021), who measured these quantities at similar redshifts in the Hubble Frontier Fields. However, the differences are not so large when considering that the fit in R. Bhatawdekar & C. J. Conselice (2021) is based on galaxies at the higher mass end, where there is a better agreement between our study and theirs.

Clearly, the scatter for points is larger in the case of the longer timescale of 100 Myr, meaning that the star formation rates for galaxies narrow at a given stellar mass for more recent star formation events in the past 10 Myr. The scatter over the shorter timescale (10 Myr) can range over a factor of $\sim$30, while for the longer timescale (100 Myr), the range is over a factor of $\sim$5.

We also find that the star formation rates are higher compared to most studies, including SFRs that are a factor of $\sim$5 higher than the $z = 9$ main sequence from HST observations (R. Bhatawdekar & C. J. Conselice 2021). In general, we see a higher star formation rate at a given mass for nearly all comparisons, with the exception of that from Y. H. Lee et al. (2019), which is roughly similar to our values, in particularly the 10 Myr star formation rate measurements.

We can also see in the sSFR panel (bottom right) of Figure 10, the red "massive" galaxies' generally have the lowest specific star formation rates, as well as the oldest ages. While star formation is still ongoing in these systems with

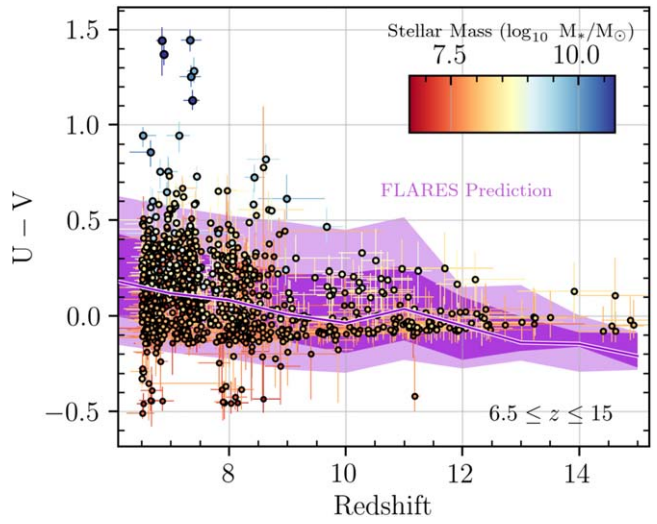

Figure 9. Plot of the rest-frame ($U - V$) color for our sample vs. redshift, colored by the stellar mass as defined in the upper-right shading. UV colors, redshift, and stellar masses are taken from the `Bagpipes` SED fitting, as discussed in Section 2.4. Uncertainties are taken from the 16th and 84th percentiles of the `Bagpipes` posterior distributions. We compare on this diagram simulation output from the FLARES simulation, showing the predicted color evolution for galaxies. The FLARES simulations are, however, only comparable down to that simulation's resolution limit, which is $M_* = 10^8\,M_\odot$.

values up to a few $M_\odot\,\mathrm{yr}^{-1}$, the relative proportion of star formation within the existing stellar masses of these galaxies is much lower than for the bursty lower-mass galaxies. The ages are also older, which is a sign that the bulk of the star formation for these red massive galaxies is much further back in time than the bluer lower-mass systems that we have in our sample. This is a firm indication that these galaxies should certainly be forming at even higher redshifts than $z = 12$, a topic that we investigate in the next Section concerning the SFHs of our sample.

3.6. Star Formation History and Stochasticity

A proper analysis of the main sequence of the distant star-forming galaxies in our sample requires knowledge of the SFHs in our sample. Predictions from both numerical simulations (e.g., G. Sun et al. 2023; T. Dome et al. 2024) and recent observational evidence from JWST (e.g., R. Endsley et al. 2023; A. Dressler et al. 2024) now support the hypothesis that star formation becomes burstier at high redshift. This is in the sense that galaxies do not have a gradual declining or increasing star formation rate with time, but that star formation happens in "bursts" whereby the star formation rate becomes rapidly higher for a relatively short period of time before declining again. This process is, in terms of time, a random one, or stochastic.

The fact that galaxies may appear to be burstier at high redshifts could be a selection bias. The reason for this is that we expect galaxies toward the detection limit of our sample to be increasingly bursty in the last 10 Myr, as these events enhance their UV luminosities, making them easier to detect and thus are included in our sample. In addition to bursty SFHs, several mini-quenched (or smoldering) galaxies with a "lull" in star formation activity with weak emission lines have been observed with JWST (T. J. Looser et al. 2023, 2024; V. Strait et al. 2023; J. Trussler et al. 2024) up at redshifts $z \sim 7$, perhaps caused by radiation-feedback driven outflows (A. Ferrara et al. 2022), bulge-formation (S. Lu et al. 2021), AGN feedback (E. J. Nelson et al. 2021), or environmental quenching processes (C. C. Williams et al. 2021).

We investigate the SFHs of our EPOCHS v1 sample by re-running through the `Bagpipes` Bayseian SED-fitting code (A. C. Carnall et al. 2018; A. Carnall 2019) with our fiducial setup, but this time adopting the nonparametric "continuity bursty" SFH model of J. Leja et al. (2019) used in both S. Tacchella et al. (2022) and T. Harvey et al. (2024). Since the wideband photometric data alone does not necessarily constrain the SFHs of individual galaxies without spectroscopic information, in Figure 12 we stack the SFHs of galaxies with both recently "rising" and "falling" SFHs, split by a star formation burstiness parameter (ϕ), which we define as:

$$\phi = (\mathrm{SFR}_{10\,\mathrm{Myr}}/\mathrm{SFR}_{100\,\mathrm{Myr}}), \quad (2)$$

with the label timescales listed being those prior to their observed epoch. There are two ways in which we use this burstiness parameter ϕ. The first is that we examine the SFH of our sample divided up into systems based on the values of ϕ, such that $\phi > 1$ are considered bursty, and $\phi < 1$ are considered non-bursty. This simple division gives us an idea of a population that has had a recent burst versus those whose star formation was higher in the relatively distant past compare with more recent star formation. What we in fact find when categorizing galaxies this way is that most of our sample consists of bursty galaxies. We find that 829 of the systems are bursty, while 225 are non-bursty. It is unclear how this should be interpreted, as we might be biased by more easily finding systems that are bursty; but at the same time, most galaxies at these higher redshifts are undergoing increasing amounts of star formation. What is likely is that we would not detect, using our existing JWST data, all of the progenitors of our bursty galaxies at higher redshifts, earlier than at the epoch than we observe them, as they would be too faint.

First, we show the SFH of each of the bursty and non-bursty systems over the time period 10–300 Myr in the left panel of Figure 12. What this shows is that the bursty systems have most of their star formation occurring later in their history, while the non-bursty galaxies have a more drawn out history.

We also show in Figure 12 the burstiness parameter as a function of both redshift and stellar mass. This distribution allows us to determine which systems are bursty, as we define this quantity above, and which have had their star formation more dominant in the relatively distant past. Figure 12 allows us to see how this parameter changes for galaxies at different redshifts and stellar masses. What is interesting is that in terms of redshift, we find that the most bursty events are all toward the lower end of our redshift range. This is another indication that samples of galaxies selected with JWST are biased toward more bursty systems. Another feature to note is that the least-massive galaxies exhibit burstier SFHs. This is the case over all redshifts, such that the higher-mass galaxies are those that have a more expanded history, and this hold at all redshifts. Whatever is producing this trend, we find that it is present up to the highest redshifts where we can find galaxies.

3.7. Ultra High-z Galaxy Properties at z > 12

One of the interesting features of our sample is that even after we check and remove the vast majority of potentially high-redshift galaxies, we are still left with a number of high-

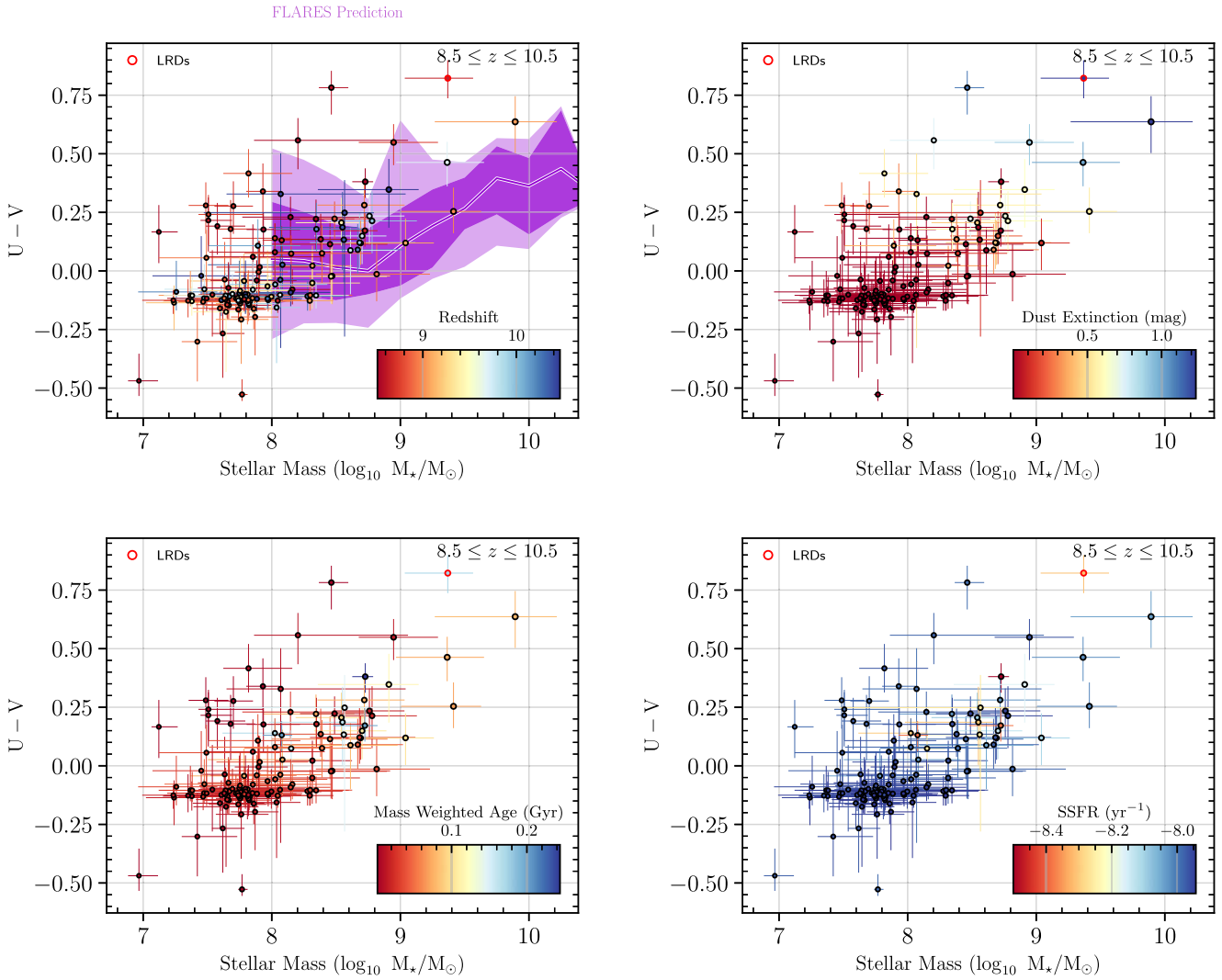

Figure 10. The relation between the stellar mass and $(U-V)$ rest-frame colors of the EPOCHS v1 sample at a relatively narrow redshift range of $8.5 < z < 10.5$ as measured with `Bagpipes`. From the top left, the markers are colored by redshift, dust extinction A_V, mass-weighted age, and specific star formation rate (sSFR). As can be seen, there are strong trends here between mass and color, and within these redder/bluer colors, there are further correlations with the star formation rate as well as the age of the stellar populations. The shaded purple region in the upper-left panel shows the FLARES prediction for these two quantities.

quality candidate ultra-high-redshift galaxies at $z > 12$. While there are now confirmations of galaxies at these high redshifts through spectroscopy (E. Curtis-Lake et al. 2022; S. Carniani et al. 2024), very few candidate galaxies at these redshifts have spectroscopic confirmation. The spectra of these systems so far are such that they generally lack emission lines or other features, beyond having a Lyman-break. Thus, even with spectroscopy, it is different to learn much about these systems, and a photometric approach using the SED fitting we have discussed is an important method for understanding these systems and how they may have formed when the Universe was less than ∼350 Myr old.

We present properties of two of these ultra-high-redshift galaxies in Figure 13. These show that the SEDs, as measured in broadband filters, are quite flat after the supposed Lyman-break. These SEDs in terms of the filters observed are not dissimilar to the spectra for similar redshift galaxies, where the continuum for these objects is flat, and there are no bright emission lines (e.g., E. Curtis-Lake et al. 2022; S. Carniani et al. 2024). These SEDs are typical for our $z > 12$ candidates, with very few showing any evidence for line emission.

At $12 < z < 15$, with the fiducial Bagpipes run, the average stellar mass for these systems is $\sim 10^8\ M_\odot$, and the average SFR using a 10 Myr timescale is $\sim 3.8\ M_\odot\,\mathrm{yr}^{-1}$. Using a 100 Myr timescale, the star formation rate is $0.9\ M_\odot\,\mathrm{yr}^{-1}$. These values are similar to what we have measured for slightly lower-redshift galaxies. It thus remains likely that many of these objects are galaxies at the edge of our current observable Universe, which future spectroscopy will confirm and allow us to study in more detail.

3.8. Galaxy Overabundance at High Redshifts

There was a great detail of excitement after the first data from JWST were analyzed showing a possible excess of distant massive and bright galaxies in comparison to simulations based on the ΛCDM framework. If indeed there are more bright and massive galaxies than expected at the highest redshifts, this could be the result of a few effects. This includes the possibility that our sample of galaxies has unusual stellar populations, a very low stellar-mass-to-light ratio, implying that even though they have a relatively low mass, they are very luminous for their mass. One possible way to accomplish this is to have

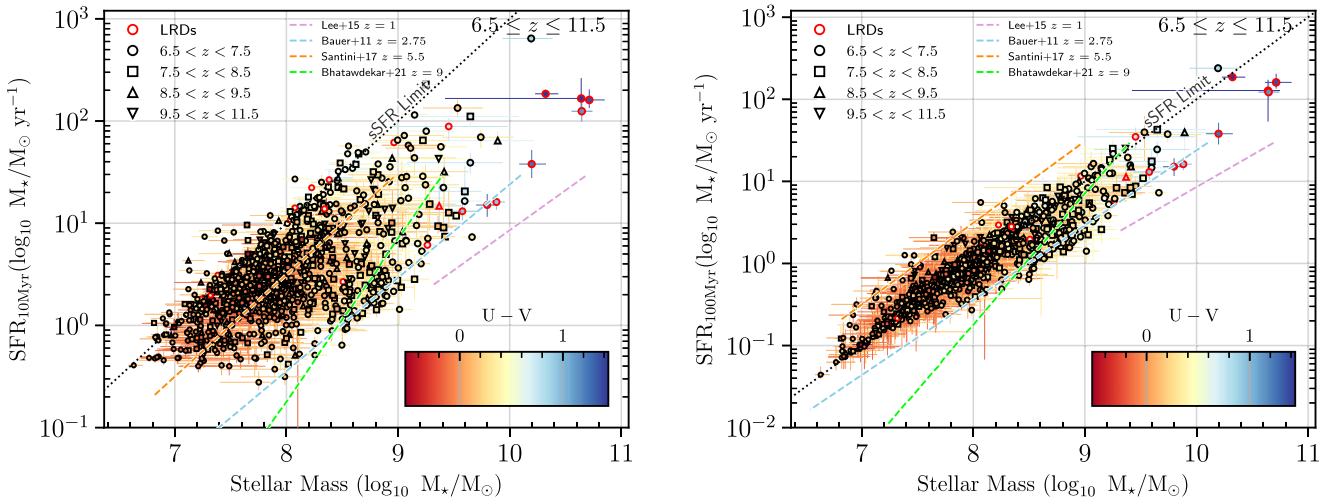

Figure 11. Star-forming main sequence from our fiducial `Bagpipes` run, shown with comparison to A. E. Bauer et al. (2011), N. Lee et al. (2015), P. Santini et al. (2017), and R. Bhatawdekar & C. J. Conselice (2021). We show average star formation on both a 100 Myr (left) and 10 Myr (right) timescale. The stellar masses and star formation rates shown have been corrected from their aperture-derived values by scaling the quantities by the ratio of the aperture-derived flux to the flux within an elliptical Kron aperture enclosing the full galaxy. We use the band closest to the rest-UV to correct the SFR, and the F444W to correct the stellar masses for aperture effects. We color the points by their rest-frame $U - V$ color, and the marker shape distinguishes the redshift bin of the galaxy. Galaxies that meet the little red dot (LRD) "red2" criteria of V. Kokorev et al. (2024) are shown with a red border, to highlight that the nature of these sources is uncertain, and the SF and stellar mass estimates shown are highly uncertain, as these systems could very well turn out to be dominated by AGNs.

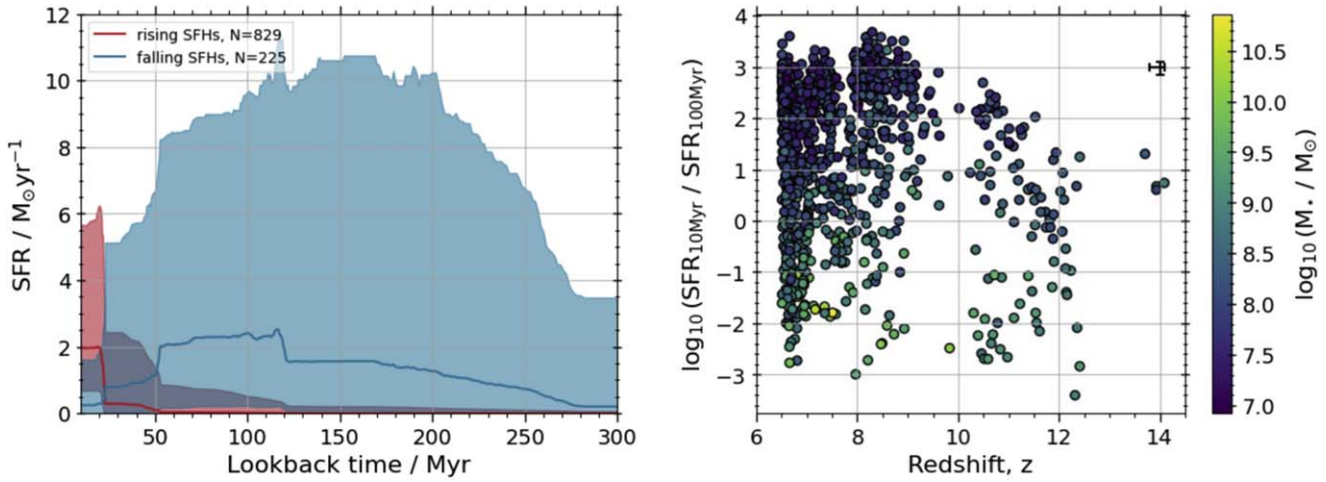

Figure 12. Plots showing the different ways in which to represent our EPOCHS sample's properties. On the left we show the distribution of SFR for two defined samples—those that have a rising star formation (in pink) and those with a falling star formation rate (in blue). The shaded areas show the 86% and 14% distribution of these values. The right panel shows the distribution of the ratio of the star formation rates within two different timescales (10 Myr) and (100 Myr) as a function of redshift. The scale shows the value of the stellar mass. A clear trend whereby the lower-mass galaxies have a burstier SFH than the higher-mass galaxies in our observed sample is apparent.

stellar populations that are dominated by high-mass stars with a top-heavy initial mass function. Alternatively, if these galaxies have stellar populations similar to lower-redshift galaxies, and if there is indeed a real excess, then there may in fact be an issue with the simulations and models that predict a higher number of systems than what we observe.

We must also consider and cannot rule out, of course, that there is the possibility that the photometric redshifts are somehow wrong; although, the vast number of galaxies with confirmed spectroscopic redshifts makes this last option more unlikely at this point (e.g., E. Curtis-Lake et al. 2022; P. Arrabal Haro et al. 2023a; S. Carniani et al. 2024). However, as mentioned, we include templates that would find objects that previous studies have incorrectly identified as high redshift. We included some discussion of the comparison of observations with theory and simulations in terms of the UV LF (distribution of UV luminosities) within N. J. Adams et al. (2024), although this comparison is largely based on the estimates of the measurement of this particular quantity, which has its own biases and incompleteness. In our study, we are able to compare directly with observations of galaxy counts, as opposed to a derived LF with all of the issues that go into constructing this accurately. We provide a more detailed study of this comparison between the data for high-redshift galaxy counts, as a function of redshift, and what the theory predicts. We thus discuss here our version of the claimed excess seen in other observations (e.g., I. Labbé et al. 2023).

In order to provide additional context for the overabundance problem, we compare our observations and fits to predictions from a variety of recent simulations. To do this, we integrate the

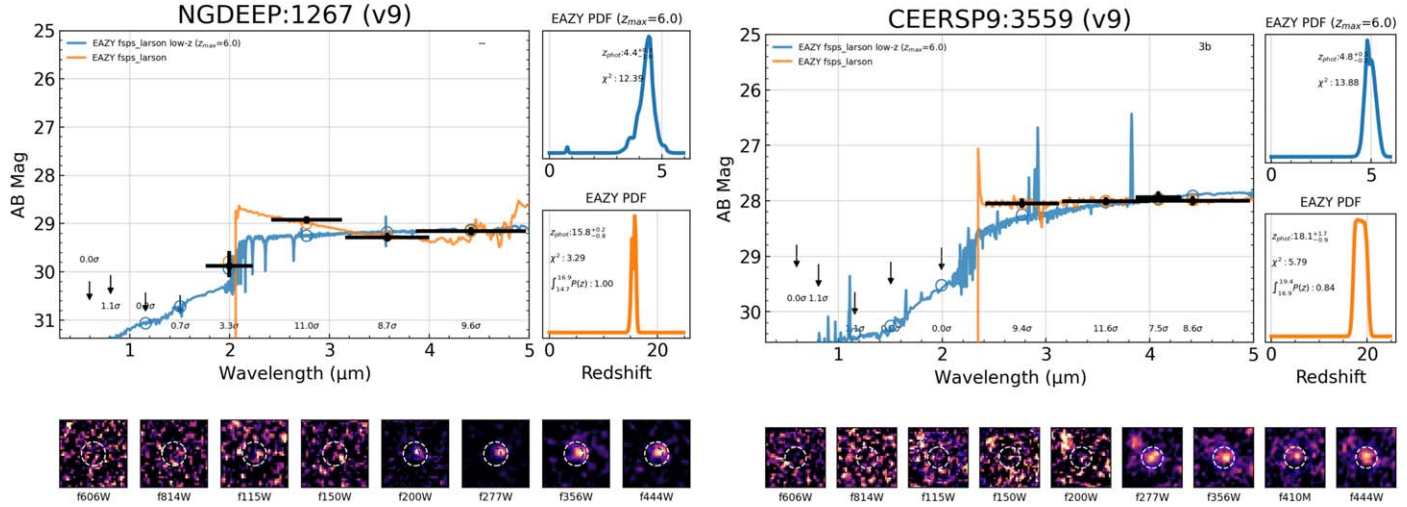

Figure 13. Example SED fits for our high-redshift galaxy candidates. Shown is the distribution and best fits, as in the previous Figures, for the lower redshifts of our sample. The left object is the NDGDEEP $z = 15.6$ galaxy discovered and first published in D. Austin et al. (2023).

predicted UV LF from various simulations: Bluetides (Y. Feng et al. 2016), Delphi (P. Dayal et al. 2014, 2022), DREAM (N. E. Drakos et al. 2022), Thesan (R. Kannan et al. 2022), the Santa Cruz semianalytic Model (L. Y. A. Yung et al. 2023), UniverseMachine (P. Behroozi et al. 2020), and FLARES (C. C. Lovell et al. 2021; A. P. Vijayan et al. 2021; S. M. Wilkins et al. 2023). Additional models also include those from P. S. Behroozi & J. Silk (2015) and A. Ferrara et al. (2022). A comparison of these simulations is illustrated in Figure 14. Integration of the LFs encompasses the rest-frame magnitude range accessible by our observations. We integrate the UV LF predicted by each model using the area and 5σ depth combination of each field used in our compilation.

A comparison of these models with our galaxy counts is shown in Figure 14. The first thing to note is that the galaxy counts with redshifts at $z < 13.5$ are higher than most models, but that a few of these, including the predictions from FLARES, Delphi, A. Ferrara et al. (2022), and the Universe-Machine do rather well in reproducing these galaxy numbers. The other models underpredict the number of galaxies compared to what we find, with only good agreements for most models at the lower redshifts at $z < 9$.

While these simulations tend to agree more with each other and with observations at these relatively lower redshifts, there is an increasing spread in their predictions toward higher redshifts. Specifically, the Delphi and FLARES simulations tend to predict greater numbers of UV faint galaxies, while Thesan and the Santa Cruz semianalytic model predict fewer of these galaxies relative to the other models. Some simulations do better than others at higher redshifts. At $z \geqslant 10$, the simulations begin to diverge in their predictions, but the observational errors also increase in this regime, making it difficult to confidently favor one physical model over another.

As can also be seen in Figure 14, there is a clear excess in the number of galaxies in our sample compared with models at $z > 12$. This is such that we are finding over an order of magnitude more galaxies in the areas of the sky we probe, than what we find in models of galaxy formation. For example, at redshift $z = 14$, we would need to have a factor of $\sim$10 fewer galaxies than what we observe to match even the highest predictions from FLARES. Within the area that we observe, this would imply that we likely would have found statistically no galaxies at these redshifts, although spectroscopy is showing that there certainly are galaxies at these epochs (S. Carniani et al. 2024).

This observation has been seen before when comparing galaxy numbers to models (N. J. Adams et al. 2024); however, we now have a large sample with robust photometric redshifts and a consistent selection methodology. While we cannot determine how significant this excess is in terms of alternative cosmological models or unusual star formation properties of distant galaxies, it does indicate that we might be seeing tension with models of galaxy formation. This is consistent to some degree with other observations, such as the rapid build-up of galaxy stellar mass early in the Universe (R. Bhatawdekar & C. J. Conselice 2021; T. Harvey et al. 2024). Future observations using JWST spectroscopy are needed to confirm our sample and determine how many of the galaxies that make up this excess are real.

4. Discussion

One of the major conclusions from our study is that with a high-fidelity sample of distant galaxies, we are able to show that there exists a great diversity in SFHs based on the photometry of these galaxies. Galaxies at $z > 6.5$ are not homogeneous at high redshift, and this is even true when we consider the effects of stellar mass, which, at lower redshifts, are typically the driving observational feature for other galaxy properties (e.g., R. Grützbauch et al. 2011). Within this paper, we also discuss a possible excess in the numbers of distant galaxies, particularly at the highest redshifts. We can interpret this excess in terms of an incorrect basis or interpretation of theory and/or observational biases.

We discuss some of these issues and what the origin of these galaxies possibly are, and what we have to look forward to once spectroscopy for these samples is obtained. One of the things to take away from this study is that not only do we find a large number of high-redshift galaxies, but that the systems at redshifts $z \sim 10$, and higher, display a great deal of diversity in their colors and stellar population properties.

We demonstrate this in several ways, including finding within a narrow redshift range, where most of our galaxies are found, that there is a great diversity of observed colors in

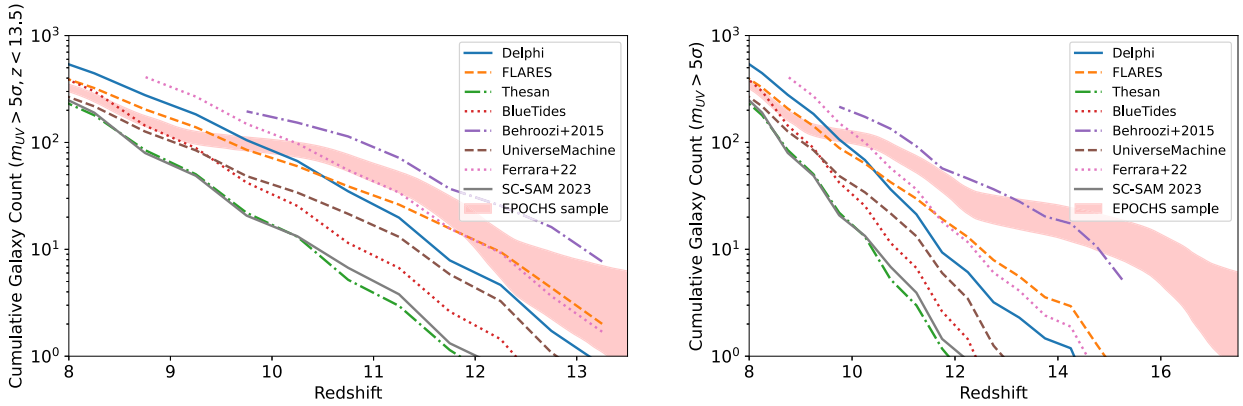

Figure 14. The cumulative number counts of very-high-redshift galaxies at $z > 8$. Here, we sum the number of galaxies detected in our fields at $5\sigma+$ in the rest-frame UV up to $z < 13.5$ (left), to match the regime of highest spectroscopic confirmations and the redshift limit employed in our other works, as well as for our full sample (right). The width of the curve derived from observations (shown in the pink shaded region) is determined by bootstrap sampling of the redshift PDFs of the sources in our sample. The shape of our observed distribution is very similar to that found in L. S. Finkelstein et al. (2022) for the CEERS field; however, CEERS only makes up a third of our volume. This shape may subsequently be a systematic caused by the choice of templates or due to the discrete wavelength sampling of JWST filters.

(F277W – F444W) versus (F150W – F277W). These colors are selected such that one color (F277W – F444W) is probing the location of the Balmer break within this redshift range, while the other probes the color of the galaxy redward of this break. From this, we can see that this color term spans a range of values from -1 to 1.5, showing a large range in the colors of our galaxies at these redshifts, which can also be seen visually when examining the SEDs of these galaxies individually (Figures 7 and 8). What this means is that the galaxies we are observing a few hundred megayears after the Big Bang contain a range of properties in their SEDs. This implies that there exists a great diversity in their star formation and merging histories (e.g., Q. Duan et al. 2024b), and within their dust content.

To understand this issue in more detail, we examine these properties of our galaxies at the same redshift range in Figure 10. We can see in this plot that indeed there is a great diversity in dust content (as fit from the SED fitting using `Bagpipes`) as well as in the ages and the sSFR values for samples at this narrow redshift range. All of this suggests that indeed there is a range in SFH, which is also seen in other properties, as described earlier and throughout this paper. While a morphological study at high redshift for these galaxies is not yet published, we know from lower redshifts at $z < 7$ that there is a great diversity of SFHs that is not accountable by overall morphology (classified as disks, ellipticals, peculiars), but which does have a trend with stellar mass (e.g., C. J. Conselice et al. 2024).

When we examine our sample in terms of stellar mass, we in fact do find some trends that suggest stellar mass is regulating the main aspects of the formation of these galaxies. We show the correlation between the stellar mass of the EPOCHS sample versus the rest-frame $(U-V)$ colors of these galaxies in Figure 10. As can be clearly seen, there is a trend, such that the more-massive galaxies are redder in this color, which can be a probe of a number of physical properties and effects, including age and dust absorption. However, this trend is not as obvious or significant at masses $M_* < 10^{8.2}\ M_\odot$ or so. Additionally, many of these more-massive systems would be considered Balmer break galaxies (e.g., J. Trussler et al. 2024). This implies that these massive systems have already undergone a significant amount of star formation, and that there is a natural break at a stellar mass of about $10^{8.2}\ M_\odot$. This is such that systems with masses lower than this have a more chaotic formation history, as the correlation of SFR with mass breaks down at this limit. In terms of the agreement with the FLARES simulation, we can use this to infer what may produce the correlation between color and stellar mass. Within FLARES, this correlation is present due to a higher dust content and higher dust density than lower-mass galaxies, due to a longer SFH, which is also backed up by our observations.

However, what we do find from our `Bagpipes` fits is that the most-massive galaxies that are red tend to have the largest dust extinctions, with A_V values approaching $A_V \sim 1$. This shows that one reason the most-massive galaxies are redder is due to the presence of dust in these systems with significant amounts of extinction. This is opposite, in some sense, to idea that some massive galaxies will be blue due to blowout of dust and other feedback effects within these galaxies. If massive galaxies become blue at these redshifts, then this phase must be short-lived (e.g., A. Ferrara et al. 2022; F. Fiore et al. 2023). These massive galaxies also appear to have, on average, lower sSFR values than galaxies at lower masses. This implies that the bulk of the star formation for these systems, as we observe them, occurs early in the history of the Universe. This is also another indication for galaxy downsizing, such that the more-massive galaxies undergo star formation earlier than lower-mass systems.

Overall, we also find that the model predictions, beyond the counts of the number of galaxies, agree reasonably well with the data. As can be seen in Figure 10, there is a good agreement between one simulation, FLARES, and that of our data for the distribution of $U-V$ color with stellar mass. The only difference is that at a given stellar mass, we find that the average value of the color is larger than that predicted, but that these are still within the range of the model. We are finding redder galaxies than those predicted, and thus it is likely that effects creating redder systems are present in the observations, but not as much in the models.

5. Conclusions

Understanding galaxy formation at the earliest times is one of the main science drivers of JWST, dictating its design and final properties. As such, there has been a considerable amount of deep imaging and spectroscopic data collected to date on both GTO and public data sets since JWST's first data releases

in July 2022. In this paper, we collate our GTO PEARLS data with a large fraction of public imaging data to construct a sample of distant galaxies at $z > 6.5$ selected with extreme care and consistently across fields, which we call the EPOCHS v1 data set. This paper describes this v1 EPOCHS data set, and we discuss the basic properties of these galaxies, focusing on their star formation rates and histories.

This EPOCHS sample is one of the largest collected from JWST observations for $z > 6.5$ galaxies to date (see also C. T. Donnan et al. 2023, 2024; Y. Harikane et al. 2023; D. J. McLeod et al. 2024), representing one of our best opportunities to study the physical properties of early galaxies. In this paper, which is the introduction to a series of papers discussing these targets and their properties (e.g., N. J. Adams et al. 2024; D. Austin et al. 2024; T. Harvey et al. 2024; Q. Li et al. 2024a), we include a general description of their discovery and features. This includes the methods by which we ensure that this sample of 1165 galaxies is robustly identified with minimal contamination.

Our results clearly show a great diversity in galaxy properties even among the most distant galaxies that JWST has discovered to date. This is shown in the vast ranges of colors, both observed as well as when comparing the rest-frame UV, for these systems. We quantify the SFH of our objects, showing that there is a large range in the SFR at 100 Myr versus 250 Myr ago. We find a general trend of downsizing, such that the most-massive galaxies at $8.5 < z < 10.5$ have the lowest specific star formation rates, the oldest ages, and the highest masses.

We also find that there is a well-defined star-forming main sequence for galaxies up to $z \sim 11.5$, such that, on average, the star formation rate increases with the stellar mass within our sample at all redshifts. We find that this trend differs from lower-redshift systems in that the star formation rates are higher compared to most studies, including SFRs that are a factor of $\sim$5 higher than the $z = 9$ main sequence from HST observations (R. Bhatawdekar & C. J. Conselice 2021).

The lower-mass galaxies in our sample have relatively large specific star formation rate, and also have young ages. This is an indication that we are seeing a trend such that the highest-mass galaxies are forming early and that the lower-mass galaxies at $z > 8.5$ still continue to undergo galaxy formation with young ages and high sSFRs at this epoch.

We find that using a rigorous selection criteria for determining which galaxies are at high redshift means that each field we study has different biases in redshift ranges. As discussed in Section 3.1 and shown in Figure 3, we find that different fields have certain redshift and magnitude biases that depend upon the filters being used within each field. This implies that using only a single field for the derivation of evolution will contain significant biases due to missing or containing fainter imaging at certain wavelengths. This is in addition to variations due to cosmic variance, which is very significant at the level of a single deep JWST imaging field. It is much better to use many different fields to carry out a more complete survey of the population of galaxies at different redshifts. However, while we find that there are biases in which redshifts we find galaxies, we do not find a bias in the colors of our galaxies within different fields. That is, overall, each field is finding similar galaxies when viewed over broad redshifts, albeit at different locations of redshift/magnitude, depending on the depth and filter coverage of the data.

We also see a generally good agreement between some galaxy properties, namely stellar mass, color, and star formation rates compared with simulations, including those from FLARES (e.g., S. M. Wilkins et al. 2022). These simulations do a good job of predicting both the colors of our galaxies up to the highest redshifts, as well as showing a good agreement between stellar mass and color. This is due to galaxies that are more massive in the simulation being relatively older systems, such that their color is redder than the more recent star-forming systems at the lower masses.

We also find that there is an apparent excess of $z > 12$ galaxies compared with models. In particular, we find that at lower redshifts, especially at $z < 10$, we find a good agreement in number densities with some simulations, although those with the highest predicted abundances are better fit than the lower value predictions. Even without a correction for incompleteness, which we do not attempt here, we are finding many more distant galaxies than are predicted in models. However, to make any stronger statements will require future JWST spectroscopy of our candidate galaxies to confirm that they are distant high-redshift galaxies.

Our results, and previous similar ones, clearly show that JWST is a powerful tool for exploring the Universe and uncovering the earliest objects. Our study of high-redshift galaxies is just the beginning, as deeper and wider imaging with JWST will greatly increase our understanding of these fundamental aspects of the Universe. We are also now acquiring Euclid data on extremely large fields, which will allow us to study the rarely brighter galaxies at the epoch of reionization (J. R. Weaver et al. 2024b). The great number of high-redshift candidates that are robust using our methods shows that further spectroscopic and imaging data on these and similar galaxies in other fields will be very revealing.

The data used in this paper and the tables of our high-z galaxies are presented in https://github.com/tHarvey303/EpochsI.

Acknowledgments

We thank the JADES, GLASS, CEERS, SMACS, and NGDEEP teams for the work in designing and preparing these public and GTO observations, and the STScI staff that carried them out. We acknowledge support from the ERC Advanced Investigator Grant EPOCHS (788113), as well three studentships from the STFC. R.A.W., S.H.C., and R.A.J. acknowledge support from NASA JWST Interdisciplinary Scientist grants NAG5-12460, NNX14AN10G, and 80NSSC18K0200 from GSFC. L.F. acknowledges financial support from Coordenação de Aperfeiçoamento de Pessoal de Nìvel Superior - Brazil (CAPES) in the form of a PhD studentship. C.C.L. acknowledges support from the Royal Society under grant RGF/EA/181016. This work is based on observations made with the NASA/ESA Hubble Space Telescope (HST) and NASA/ESA/CSA James Webb Space Telescope (JWST) obtained from the Mikulski Archive for Space Telescopes (MAST) at the Space Telescope Science Institute (STScI), which is operated by the Association of Universities for Research in Astronomy, Inc., under NASA contract NAS 5-03127 for JWST, and NAS 5-26555 for HST. The specific observations analyzed can be accessed via doi:10.17909/5h64-g193.

This research made use of the following Python libraries: ASTROPY (Astropy Collaboration et al. 2022);

MORFOMETRYKA (F. Ferrari et al. 2015); PANDAS (T. pandas development team 2020); MATPLOTLIB (J. D. Hunter 2007); PHOTUTILS (L. Bradley et al. 2022).

Appendix A
Table of Galaxy Properties

In this Appendix, we provide more information on the data release for our objects found as part of the EPOCHS v1 catalog. We give a description of how our objects are identified and give a description of the properties that are contained within the released catalog for the EPOCHS sample. A list of the quantities we provide in the catalog is presented in Table 4. Included within our released catalog are the basic properties of 1165 EPOCHS v1 galaxies. This includes their photometry in the JWST filters and, when available, HST ACS data. We also include other derived properties based on this photometry. These include the photometric redshift, the stellar mass measured in different ways (see T. Harvey et al. 2024 for more information on how masses are measured), as well as the various age measurements from Bagpipes. In terms of derived quantities, we also gives values for the UV β slope (D. Austin et al. 2024), the dust and metallicty values, as well as derived absolute magnitudes $M_{UV,}$ and the rest-frame $(U-V)$ colors. Within this Table, we also provide values for the uncertainties on these quantities.

Table 4
EPOCHS v1 Catalog Column Names, Units, Descriptions, and Column Shape, Specifically for the Stellar Population Parameters Calculated Using `Bagpipes`

Column Name	Unit	Description
Fiducial `Bagpipes` Results (z_{fix} or z_{Gauss})		
redshift_pipes_zgauss		Fitted redshift (zgauss only)
redshift_pipes_l1_zgauss		Lower uncertainty (50th - 16th percentile)
redshift_pipes_u1_zgauss		Upper uncertainty (84th - 50th percentile)
stellar_mass_pipes_EXT*	$\log_{10}(M_\odot)$	Total surviving stellar mass
stellar_mass_pipes_l1_EXT	$\log_{10}(M_\odot)$	Lower uncertainty (50th - 16th percentile)
stellar_mass_pipes_u1_EXT	$\log_{10}(M_\odot)$	Upper uncertainty (84th - 50th percentile)
SFR_10Myr_pipes_EXT*	$M_\odot$ yr^{-1}	Average total star formation rate over a 10 Myr timescale
SFR_10Myr_pipes_l1_EXT	$M_\odot$ yr^{-1}	Lower uncertainty (50th - 16th percentile)
SFR_10Myr_pipes_u1_EXT	$M_\odot$ yr^{-1}	Upper uncertainty (84th - 50th percentile)
SFR_100Myr_pipes_EXT*	$M_\odot$ yr^{-1}	Average total star formation rate over a 100 Myr timescale
SFR_100Myr_pipes_l1_EXT	$M_\odot$ yr^{-1}	Lower uncertainty (50th - 16th percentile)
SFR_100Myr_pipes_u1_EXT	$M_\odot$ yr^{-1}	Upper uncertainty (84th - 50th percentile)
mass_weighted_age_pipes_EXT	Myr	Mass-weighted age of galaxy
mass_weighted_age_pipes_l1_EXT	Myr	Lower uncertainty (50th - 16th percentile)
mass_weighted_age_pipes_u1_EXT	Myr	Upper uncertainty (84th - 50th percentile)
beta_pipes_EXT		UV β slope of best-fitting `Bagpipes` spectra in Calzetti filters
beta_pipes_l1_EXT		Lower uncertainty (50th - 16th percentile)
beta_pipes_u1_EXT		Upper uncertainty (84th - 50th percentile)
Z_star_pipes_EXT	$Z_\odot$	Stellar metallicity
Z_star_pipes_l1_EXT	$Z_\odot$	Lower uncertainty (50th - 16th percentile)
Z_star_pipes_u1_EXT	$Z_\odot$	Upper uncertainty (84th - 50th percentile)
A_V_pipes_EXT	AB mag	Dust extinction in the V band
A_V_pipes_l1_EXT	AB mag	Lower uncertainty (50th - 16th percentile)
A_V_pipes_u1_EXT	AB mag	Upper uncertainty (84th - 50th percentile)
U-V_pipes_EXT	AB mag	U-V color
U-V_pipes_l1_EXT	AB mag	Lower uncertainty (50th - 16th percentile)
U-V_pipes_u1_EXT	AB mag	Upper uncertainty (84th - 50th percentile)
M_UV_pipes_EXT	AB mag	Absolute UV Magnitude
M_UV_pipes_l1_EXT	AB mag	Lower uncertainty (50th - 16th percentile)
M_UV_pipes_u1_EXT	AB mag	Upper uncertainty (84th - 50th percentile)
chisq_phot_pipes_EXT		χ^2 of fit

Note. "EXT" indicates that the column name appears multiple times with different extensions, and in this case, "EXT" can take the value of zfix or zgauss, depending on whether the redshift is fixed to the EAZY maximum likelihood result given by "zbest," or allowed to vary within a Gaussian centered on "zbest." Those entries with an "$\star$" indicate that the column has been corrected for any flux associated with the galaxy that falls outside the extraction aperture. For masses, this is done by correcting the mass by the ratio of MAG-AUTO to MAG-APER in the longest-wavelength F444W band, where this exceeds unity. For star formation rates, the band covering the rest-frame 1500 Å wavelength is used instead.

Appendix B
Completeness and Contamination Simulation Results

As described in the main text of this paper, we carry out a series of simulations of our fields to determine the contamination and completeness for detecting galaxies within each of the fields we use. Completeness is important, as we want to detect and measure as many galaxies at a given brightness and redshift as we can. Thus, we aim to have completeness values approach unity. Contamination is also important to minimize, as it is possible to have a very generous selection method that results in a sample that is very complete, but is full of contamination from objects at other redshifts. Thus, our goal is to minimize the contamination with values approaching zero while maximizing the completeness.

As the depths and filters and other properties of our fields differ significantly between each other, carrying out these simulations is necessary to determine the limits of where we can use data in each field while retaining a high purity. These simulations are such that we can determine whether or not a galaxy in the JAGUAR simulation would be detected. We examine this as a function of galaxy brightness, which we convert into an absolute magnitude, at a given redshift. From this, we can determine, using our EPOCHS criteria, how many of these galaxies are within a bin of redshift and absolute magnitude compared to the total number placed in that bin.

In Figure 15, we show plots of both the completeness and contamination for each our EPOCHS fields. These are plotted as a function of redshift and the UV absolute magnitude. We define the completeness as the number of galaxies within the JAGUAR simulation of each field that we retrieve through our methods of identifying high-redshift galaxies, which we call N(true-positive) divided by the total number of galaxies in the true sample from JAGUAR with known redshifts based on the simulation, which we call N(total). This value is given by the completeness $C(z)$:

$$C(z) = \frac{N(\text{true} - \text{positives(z)})}{N(\text{total(z)})} \tag{B1}$$

whereby for the contamination $K(z)$, we calculate this value by the formula

$$K(z) = \frac{N(\text{false} - \text{positives(z)})}{N(\text{obs(z)})}. \tag{B2}$$

This is such that the value N(false-positives(z)) is the number of objects detected by our methods that are not at the correct redshift as given by the JAGUAR catalog. The various completeness and contamination values for each of our fields are shown in Figure 15. As can be seen in this Figure, our fields have a variety of completeness levels that vary with both the absolute magnitude and redshift. In general, those that have a larger amount of darker colors in the completeness (left-hand side) have a higher completeness at a fainter magnitude. The deepest surveys JADES and NGDEEP are both complete to nearly 100% down to apparent UV magnitudes of 29–29.3. Our shallower fields, including Clio and SMACS 0723 have more structure in their completeness, such that at higher redshifts, the detection process is more complete up to magnitudes of 28–28.5, but have a higher incompleteness at the lower redshifts. This is due to the nature of the lower-redshift galaxies being rejected on one or more of our criteria, often due to the limited wavelength coverage around the wavelength of the Lyman-break.

The contamination shown on the right panels of Figure 15 is also quite interesting and shows trends that differ slightly between fields. For the deepest fields, the contamination is very low, close to zero up to magnitude $m = 29$. However, for these fields, including JADES and NGDEEP, the contamination becomes quite high at about 50% between magnitudes 29–30 for the highest-redshift galaxies, which are detected at redshifts $z \sim 11$–13. Therefore, at this faint galaxy range at these higher redshifts, caution should be taken when analyzing galaxies selected.

Contamination increases at fainter magnitudes within other fields, including NEP-TDF, CEERS, and GLASS at magnitudes fainter than 28. The other PEARLS fields have a contamination that starts to become high at even fainter limits, around magnitude 27, implying that only the brightest magnitudes should be used to construct samples from these fields.

These simulation results become much less certain as we go higher in redshift. This is the reason why we combine multiple iterations of the JAGUAR simulation to construct a sample that has a large enough number of the most distant galaxies. By the time we reach $z = 12$, there are only a few sources to examine within this simulation. Given the current state of mocks, this is however the best we can do, which is also the reason why we cannot perform these tests at the highest redshifts our data probes.

The objects that produce contamination in the simulation are typically galaxies with strong emission lines and a relatively small Balmer break. Generally, the F090W, F115W, and F150W bands are 0.3–0.4 magnitudes shallower than in those bands where we detect these sources (F200W, F277W, F356W). This implies that objects detected at a 5σ–8σ level in the rest-frame UV do not have deep enough blue-band data to confirm if a nondetection is truly due to a Lyman-break or a Balmer break. The placement of strong Hβ/[O III] and Hα in these broad bands often makes galaxy SEDs appear bluer than expected.

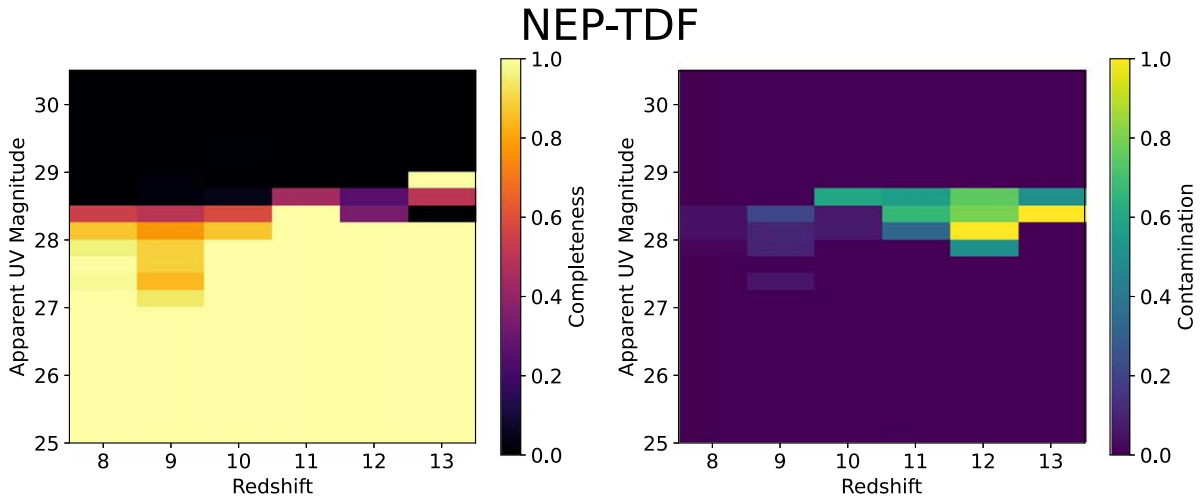

(a) Completeness and contamination for the NEP-TDF field.

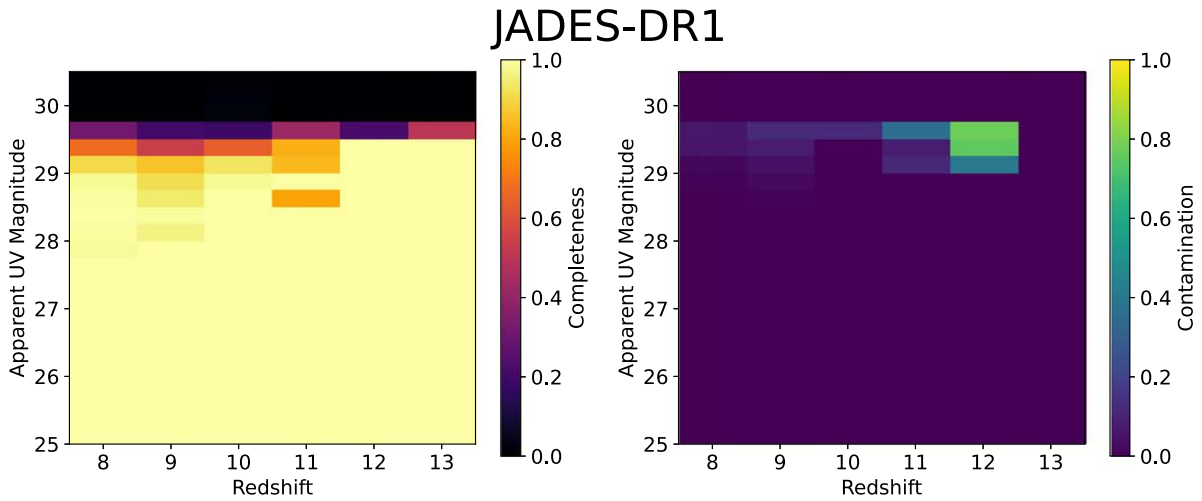

(b) Completeness and contamination for the JADES GOODS-S survey.

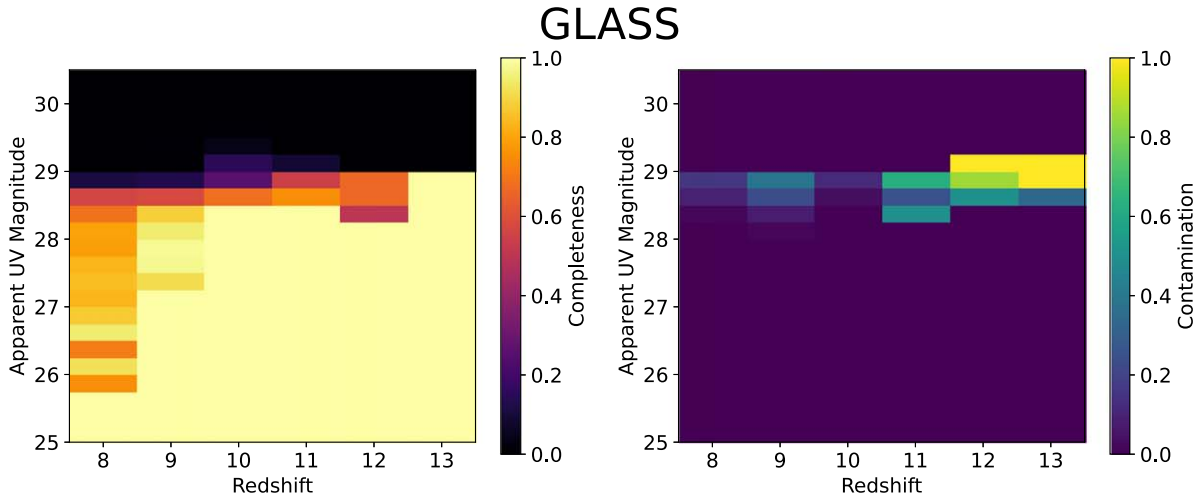

(c) Completeness and contamination for the GLASS survey.

Figure 15. The selection completeness $C(z)$ and contamination ($K(z)$ simulation results conducted using the JAGUAR semianalytical model using the conditions for each survey setup. The color bar shows the fractional completeness recovered and the contamination fraction of objects with $z < 5$ entering the sample. This is used to form the completeness factor C in Equation (B1), and K in Equation (B2).

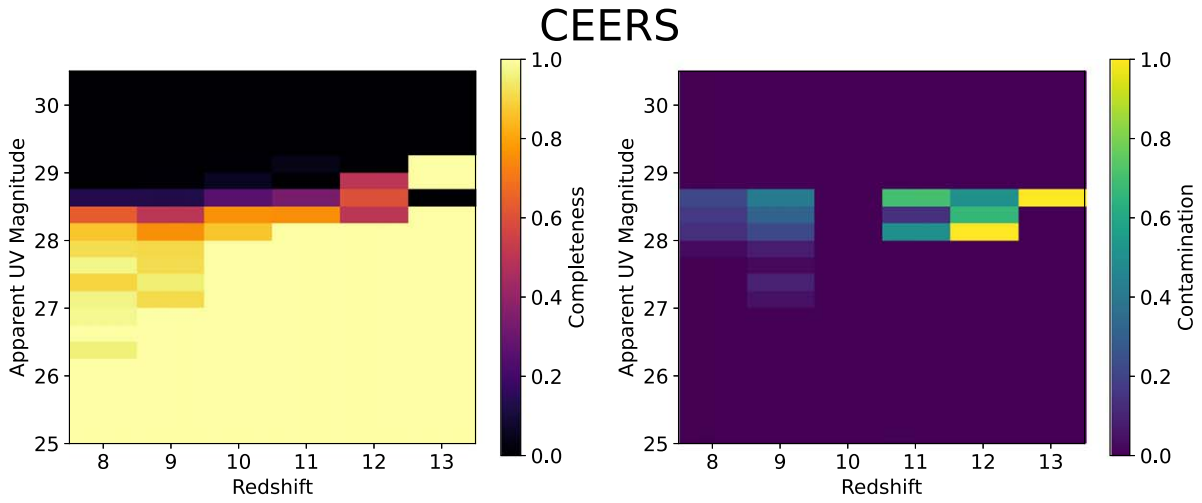

(d) Completeness and contamination for the CEERS survey in the EGS region.

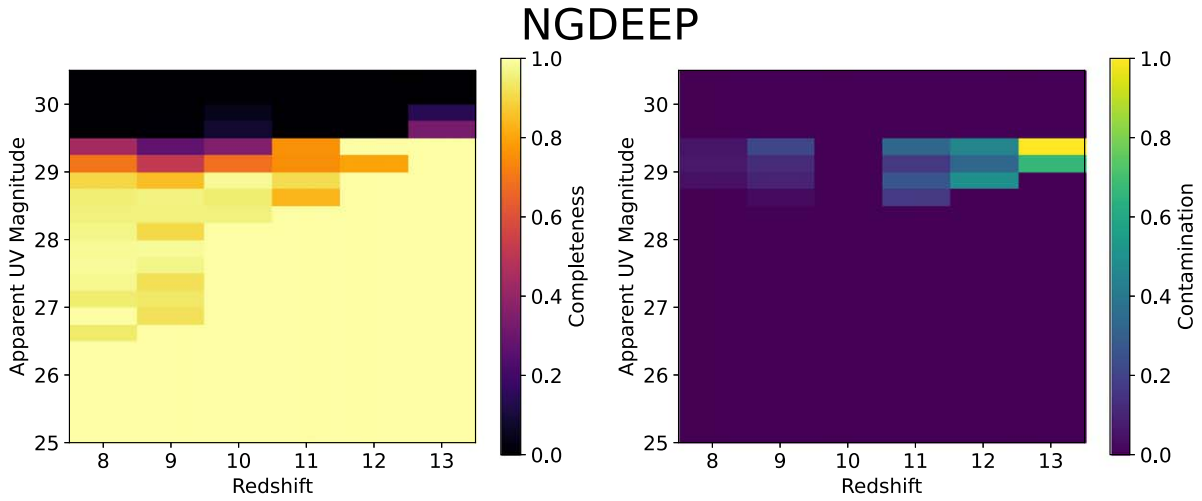

(e) Completeness and contamination for the NGDEEP survey.

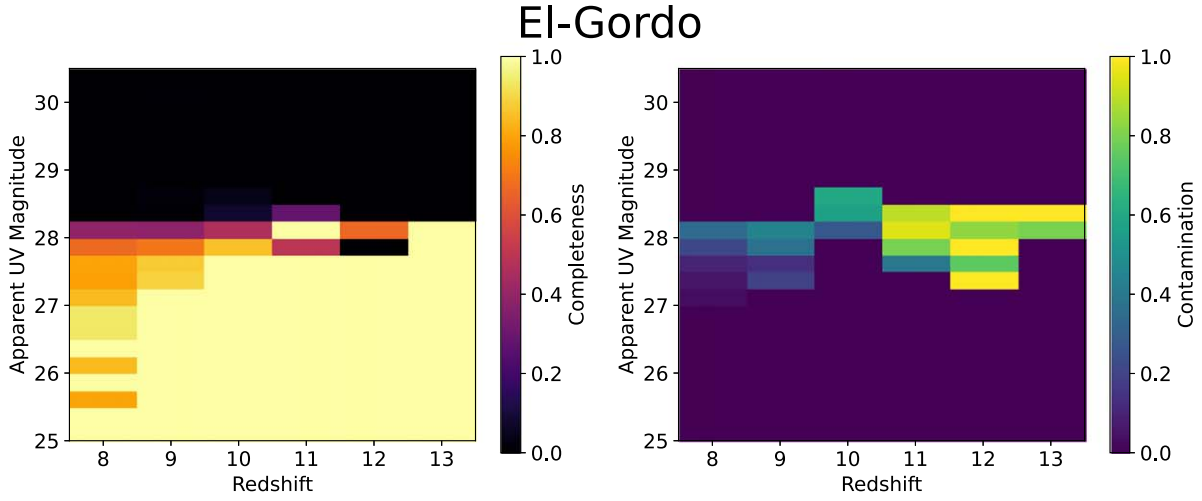

(f) Completeness and contamination for the El Gordo field, which does not include the cluster region.

Figure 15. (Continued.)

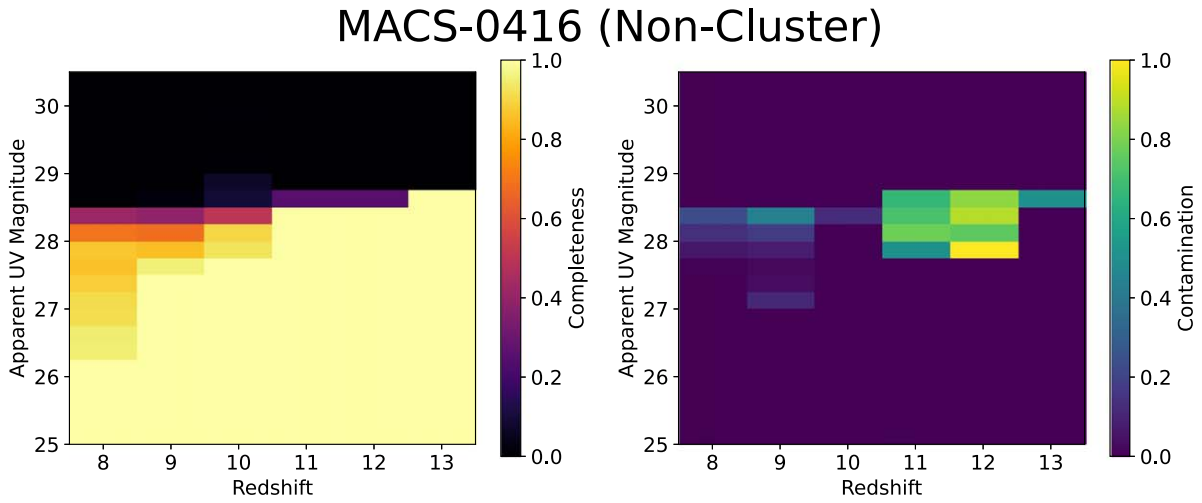

(g) Completeness and contamination for the M0416 cluster region. The cluster region itself is not included in this.

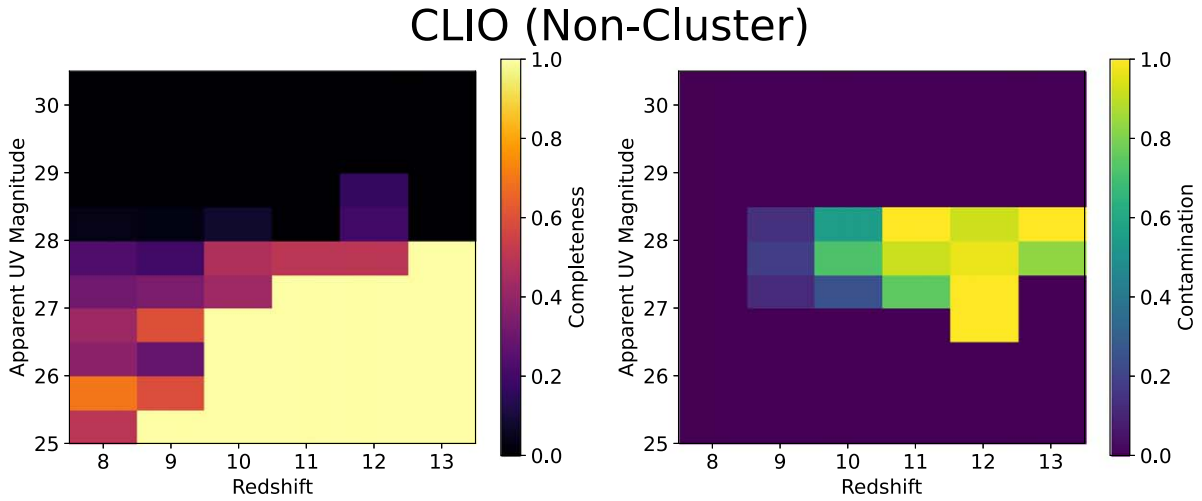

(h) Completeness and contamination for the Clio cluster area. The cluster region itself is not included in this.

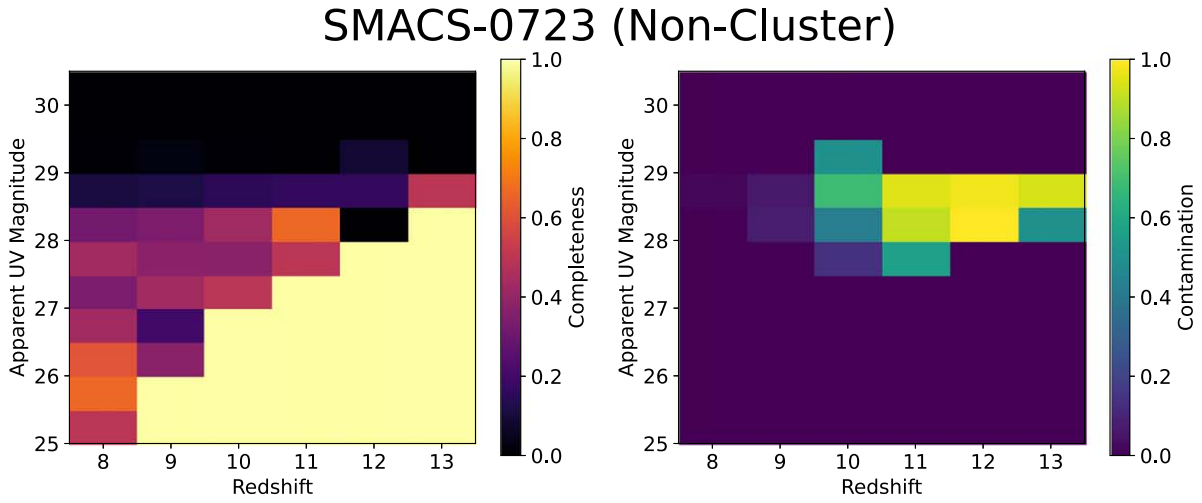

(i) Completeness and contamination for the SMACS-0723 cluster region outside the main cluster.

Figure 15. (Continued.)

ORCID iDs

Christopher J. Conselice https://orcid.org/0000-0003-1949-7638
Nathan Adams https://orcid.org/0000-0003-4875-6272
Thomas Harvey https://orcid.org/0000-0002-4130-636X
Duncan Austin https://orcid.org/0000-0003-0519-9445
Katherine Ormerod https://orcid.org/0000-0003-2000-3420
Qiao Duan https://orcid.org/0009-0009-8105-4564
James Trussler https://orcid.org/0000-0002-9081-2111
Qiong Li https://orcid.org/0000-0002-3119-9003
Ignas Juodžbalis https://orcid.org/0009-0003-7423-8660
Lewi Westcott https://orcid.org/0009-0008-8642-5275
Honor Harris https://orcid.org/0009-0005-0817-6419
Louise T. C. Seeyave https://orcid.org/0000-0002-7020-3079
Asa F. L. Bluck https://orcid.org/0000-0001-6395-4504
Rogier A. Windhorst https://orcid.org/0000-0001-8156-6281
Rachana Bhatawdekar https://orcid.org/0000-0003-0883-2226
Dan Coe https://orcid.org/0000-0001-7410-7669
Seth H. Cohen https://orcid.org/0000-0003-3329-1337
Cheng Cheng https://orcid.org/0000-0003-0202-0534
Simon P. Driver https://orcid.org/0000-0001-9491-7327
Brenda Frye https://orcid.org/0000-0003-1625-8009
Lukas J. Furtak https://orcid.org/0000-0001-6278-032X
Norman A. Grogin https://orcid.org/0000-0001-9440-8872
Nimish P. Hathi https://orcid.org/0000-0001-6145-5090
Benne W. Holwerda https://orcid.org/0000-0002-4884-6756
Rolf A. Jansen https://orcid.org/0000-0003-1268-5230
Anton M. Koekemoer https://orcid.org/0000-0002-6610-2048
Madeline A. Marshall https://orcid.org/0000-0001-6434-7845
Mario Nonino https://orcid.org/0000-0001-6342-9662
Aaron Robotham https://orcid.org/0000-0003-0429-3579
Jake Summers https://orcid.org/0000-0002-7265-7920
Stephen M. Wilkins https://orcid.org/0000-0003-3903-6935
Christopher N. A. Willmer https://orcid.org/0000-0001-9262-9997
Haojing Yan https://orcid.org/0000-0001-7592-7714
Adi Zitrin https://orcid.org/0000-0002-0350-4488

References

Adams, N. J., Conselice, C. J., Austin, D., et al. 2024, ApJ, 965, 169
Adams, N. J., Conselice, C. J., Ferreira, L., et al. 2023, MNRAS, 518, 4755
Arrabal Haro, P., Dickinson, M., Finkelstein, S. L., et al. 2023a, Natur, 622, 707
Arrabal Haro, P., Dickinson, M., Finkelstein, S. L., et al. 2023b, ApJL, 951, L22
Astropy Collaboration, Price-Whelan, A. M., Lim, P. L., et al. 2022, ApJ, 935, 167
Atek, H., Shuntov, M., Furtak, L. J., et al. 2023, MNRAS, 519, 1201
Austin, D., Adams, N., Conselice, C. J., et al. 2023, ApJL, 952, L7
Austin, D., Conselice, C. J., Adams, N. J., et al. 2024, arXiv: 2404.10751
Bagley, M. B., Pirzkal, N., Finkelstein, S. L., et al. 2024, ApJ, 965, 6L
Bauer, A. E., Conselice, C. J., Pérez-González, P. G., et al. 2011, MNRAS, 417, 289
Behroozi, P., Conroy, C., Wechsler, R. H., et al. 2020, MNRAS, 499, 5702
Behroozi, P. S., & Silk, J. 2015, ApJ, 799, 32
Bertin, E., & Arnouts, S. 1996, A&AS, 117, 393
Bhatawdekar, R., & Conselice, C. J. 2021, ApJ, 909, 144
Bouwens, R. J., Aravena, M., Decarli, R., et al. 2016, ApJ, 833, 72
Bouwens, R. J., Illingworth, G. D., Labbe, I., et al. 2011, Natur, 469, 504
Bowler, R. A. A., Jarvis, M. J., Dunlop, J. S., et al. 2020, MNRAS, 493, 2059
Bradley, L., Sipocz, B., Robitaille, T., et al. 2022, astropy/photutils: 1.5.0, Zenodo, doi:10.5281/zenodo.6825092
Brammer, G. B., van Dokkum, P. G., & Coppi, P. 2008, ApJ, 686, 1503
Bruzual, G., & Charlot, S. 2003, MNRAS, 344, 1000
Bunker, A. J., Cameron, A. J., Curtis-Lake, E., et al. 2024, A&A, 690, A288
Bushouse, H., Eisenhamer, J., Dencheva, N., et al. 2022, JWST Calibration Pipeline, Zenodo, Zenodo: 10.5281/ZENODO.7325378
Byrne, C. M., Stanway, E. R., Eldridge, J. J., McSwiney, L., & Townsend, O. T. 2022, MNRAS, 512, 5329
Calzetti, D., Armus, L., Bohlin, R. C., et al. 2000, ApJ, 533, 682
Carnall, A. 2019, The Art of Measuring Galaxy Physical Properties, 44
Carnall, A. C., Begley, R., McLeod, D. J., et al. 2023, MNRAS, 518, L45
Carnall, A. C., McLure, R. J., Dunlop, J. S., & Davé, R. 2018, MNRAS, 480, 4379
Carniani, S., Hainline, K., D'Eugenio, F., et al. 2024, Natur, 633, 318
Castellano, M., Fontana, A., Treu, T., et al. 2022, ApJL, 938, L15
Castellano, M., Napolitano, L., Fontana, A., et al. 2024, ApJ, 972, 143
Chakraborty, P., Sarkar, A., Wolk, S., et al. 2024, arXiv: 2406.05306
Conroy, C., & Gunn, J. E., 2010 FSPS: Flexible Stellar Population Synthesis, Astrophysics Source Code Library, ascl:1010.043
Conselice, C. J., Basham, J. T. F., Bettaney, D. O., et al. 2024, MNRAS, 531, 4857
Conselice, C. J., Mundy, C. J., Ferreira, L., & Duncan, K. 2022, ApJ, 940, 168
Curtis-Lake, E., Carniani, S., Cameron, A., et al. 2023, NatAs, 7, 622
Dayal, P., Ferrara, A., Dunlop, J. S., & Pacucci, F. 2014, MNRAS, 445, 2545
Dayal, P., Ferrara, A., Sommovigo, L., et al. 2022, MNRAS, 512, 989
D'Eugenio, F., Cameron, A. J., Scholtz, J., et al. 2025, ApJS, 277, 4
Dome, T., Tacchella, S., Fialkov, A., et al. 2024, MNRAS, 527, 2139
Donnan, C. T., McLeod, D. J., Dunlop, J. S., et al. 2023, MNRAS, 518, 6011
Donnan, C. T., McLure, R. J., Dunlop, J. S., et al. 2024, MNRAS, 533, 3222
Drakos, N. E., Villasenor, B., Robertson, B. E., et al. 2022, ApJ, 926, 194
Dressler, A., Rieke, M., Eisenstein, D., et al. 2024, ApJ, 964, 150
Duan, Q., Conselice, C. J., Li, Q., et al. 2024a, MNRAS, 529, 4728
Duan, Q., Conselice, C. J., Li, Q., et al. 2024b, arXiv: 2407.09472
Duncan, K., Conselice, C. J., Mundy, C., et al. 2019, ApJ, 876, 110
Eisenstein, D. J., Willott, C., Alberts, S., et al. 2023, arXiv: 2306.02465
Eldridge, J. J., Stanway, E. R., Xiao, L., et al. 2017, PASA, 34, e058
Ellis, R. S., McLure, R. J., Dunlop, J. S., et al. 2013, ApJL, 763, L7
Endsley, R., Stark, D. P., Whitler, L., et al. 2024, MNRAS, 533, 1111
Feng, Y., Di-Matteo, T., Croft, R. A., et al. 2016, MNRAS, 455, 2778
Ferrara, A., Pallottini, A., & Dayal, P. 2022, MNRAS, 522, 3986
Ferrari, F., de Carvalho, R. R., & Trevisan, M. 2015, ApJ, 814, 55
Ferreira, L., Adams, N., Conselice, C. J., et al. 2022, ApJL, 938, L2
Finkelstein, L. S., Bagley, M. B., Arrabal Haro, P., et al. 2022, ApJL, 940, L55
Finkelstein, S. L., Bagley, M. B., Ferguson, H. C., et al. 2023, ApJL, 946, L13
Finkelstein, S. L., Leung, G. C. K., Bagley, M. B., et al. 2024, ApJL, 969, L2
Fiore, F., Ferrara, A., Bischetti, M., Feruglio, C., & Travascio, A. 2023, ApJL, 943, L27
Frye, B. L., Pascale, M., Pierel, J., et al. 2024, ApJ, 961, 171
Fu, K. L. K., Conselice, C. J., Ferreira, L., et al. 2024, arXiv: 2403.18458
Fujimoto, S., Haro, P. A., Dickinson, M., et al. 2023, ApJL, 949, L25
Gaia Collaboration, Vallenari, A., Brown, A. G. A., et al. 2022, arXiv: 2208.00211
Glazebrook, K., Nanayakkara, T., Schreiber, C., et al. 2024, Natur, 628, 277
Griffiths, A., Conselice, C. J., Alpaslan, M., et al. 2018, MNRAS, 475, 2853
Grogin, N. A., Kocevski, D. D., Faber, S. M., et al. 2011, ApJS, 197, 35
Grützbauch, R., Conselice, C. J., Bauer, A. E., et al. 2011, MNRAS, 418, 938
Hainline, K. N., Johnson, B. D., Robertson, B., et al. 2024a, ApJ, 964, 71
Hainline, K. N., Helton, J. M., Johnson, B. D., et al. 2024b, ApJ, 964, 66
Harikane, Y., Inoue, A. K., Mawatari, K., et al. 2022, ApJ, 929, 1
Harikane, Y., Nakajima, K., Ouchi, M., et al. 2024, ApJ, 960, 56
Harikane, Y., Ouchi, M., Oguri, M., et al. 2023, ApJS, 265, 5
Harvey, T., Conselice, C., Adams, N. J., et al. 2025, ApJ, 978, 89
Hoaglin, D. C., Mosteller, F., & Tukey, J. W. 1983, Understanding Robust and Exploratory Data Analysis (New York: Wiley)
Hunter, J. D. 2007, CSE, 9, 90
Illingworth, G., Magee, D., Bouwens, R., et al. 2016, arXiv: 1606.00841
Juodžbalis, I., Conselice, C. J., Singh, M., et al. 2023, MNRAS, 525, 1353
Kannan, R., Garaldi, E., Smith, A., et al. 2022, MNRAS, 511, 4005
Karalidi, T., Marley, M., Fortney, J. J., et al. 2021, ApJ, 923, 269
Koekemoer, A. M., Faber, S. M., Ferguson, H. C., et al. 2011, ApJS, 197, 36
Kokorev, V., Caputi, K. I., Greene, J. E., et al. 2024, ApJ, 968, 38
Kragh Jespersen, C., Steinhardt, C. L., Somerville, R. S., & Lovell, C. C. 2025, ApJ, 982, 23
Kron, R. G. 1980, ApJS, 43, 305
Labbé, I., van Dokkum, P., Nelson, E., et al. 2023, Natur, 616, 266

Larson, R. L., Finkelstein, S. L., Kocevski, D. D., et al. 2023, ApJL, 953, L29
Larson, R. L., Hutchison, T. A., Bagley, M., et al. 2023, ApJ, 958, 141L
Lee, N., Sanders, D. B., Casey, C. M., et al. 2015, ApJ, 801, 80
Lee, Y. H., Ann, H. B., & Park, M.-G. 2019, ApJ, 872, 97
Leja, J., Carnall, A. C., Johnson, B. D., Conroy, C., & Speagle, J. S. 2019, ApJ, 876, 3
Leung, G. C. K., Bagley, M. B., Finkelstein, S. L., et al. 2023, ApJL, 954, L46
Li, Q., Conselice, C. J., Adams, N., et al. 2024a, MNRAS, 531, 617
Li, Q., Conselice, C. J., Sarron, F., et al. 2024b, arXiv: 2405.17359
Looser, T. J., D'Eugenio, F., Maiolino, R., et al. 2023, arXiv: 2306.02470
Looser, T. J., D'Eugenio, F., Maiolino, R., et al. 2024, Natur, 629, 53
Lovell, C. C., Vijayan, A. P., Thomas, P. A., et al. 2021, MNRAS, 500, 2127
Lu, S., Fang, G., Gu, Y., et al. 2021, ApJ, 913, 81
Ma, Z., Sun, B., Cheng, C., et al. 2024, ApJ, 975, 87
Madau, P. 1995, ApJ, 441, 18
Madau, P., & Dickinson, M. 2014, ARA&A, 52, 415
Marley, M. S., Saumon, D., Visscher, C., et al. 2021, ApJ, 920, 85
McLeod, D. J., Donnan, C. T., McLure, R. J., et al. 2024, MNRAS, 527, 5004
McLeod, D. J., McLure, R. J., & Dunlop, J. S. 2016, MNRAS, 459, 3812
Morishita, T., Trenti, M., Stiavelli, M., et al. 2018, ApJ, 867, 150
Moster, B. P., Somerville, R. S., Newman, J. A., & Rix, H.-W. 2011, ApJ, 731, 113
Mundy, C. J., Conselice, C. J., Duncan, K. J., et al. 2017, MNRAS, 470, 3507
Nabizadeh, A., Zackrisson, E., Pacucci, F., et al. 2024, A&A, 683, A58
Naidu, R. P., Oesch, P. A., van Dokkum, P., et al. 2022, ApJL, 940, L14
Nelson, E. J., Tacchella, S., Diemer, B., et al. 2021, MNRAS, 508, 219
Noeske, K. G., Weiner, B. J., Faber, S. M., et al. 2007, ApJL, 660, L43
O'Brien, R., Jansen, R. A., Grogin, N. A., et al. 2024, ApJS, 272, 19
Oesch, P. A., Bouwens, R. J., Illingworth, G. D., Labbé, I., & Stefanon, M. 2018, ApJ, 855, 105
Oesch, P. A., Bouwens, R. J., Illingworth, G. D., et al. 2014, ApJ, 786, 108
Oke, J. B. 1974, ApJS, 27, 21
Oke, J. B., & Gunn, J. E. 1983, ApJ, 266, 713
Ormerod, K., Conselice, C. J., Adams, N. J., et al. 2024, MNRAS, 527, 6110
Pacifici, C., Iyer, K. G., Mobasher, B., et al. 2023, ApJ, 944, 141
pandas development team, T. 2020, pandas-dev/pandas: Pandas, Zenodo, doi:10.5281/zenodo.3509134
Pérez-González, P. G., Costantin, L., Langeroodi, D., et al. 2023, ApJL, 951, L1
Perrin, M. D., Sivaramakrishnan, A., Lajoie, C.-P., et al. 2014, Proc. SPIE, 9143, 91433X
Perrin, M. D., Soummer, R., Elliott, E. M., Lallo, M. D., & Sivaramakrishnan, A. 2012, Proc. SPIE, 8442, 84423D
Pontoppidan, K., Barrientes, J., Blome, C., et al. 2022, ApJ, 936, L14
Rieke, G. H., Wright, G. S., Böker, T., et al. 2015, PASP, 127, 584
Rieke, M., Kelly, D., Horner, S. & NIRCam Team 2005, AAS Meeting, 207, 115.09
Rieke, M. J., Eisenstein, D., Engelbracht, C. W., et al. 2008, AAS Meeting, 212, 79.01
Rieke, M. J., Robertson, B., Tacchella, S., et al. 2023, ApJS, 269, 16
Rigby, J., Perrin, M., McElwain, M., et al. 2023, PASP, 135, 048001
Salmon, B., Coe, D., Bradley, L., et al. 2018, ApJL, 864, L22
Santini, P., Fontana, A., Castellano, M., et al. 2017, ApJ, 847, 76
Sarron, F., & Conselice, C. J. 2021, MNRAS, 506, 2136
Stanway, E. R., & Eldridge, J. J. 2018, MNRAS, 479, 75
Stefanon, M., Labbé, I., Bouwens, R. J., et al. 2019, ApJ, 883, 99
Steidel, C. C., & Hamilton, D. 1992, AJ, 104, 941
Strait, V., Brammer, G., Muzzin, A., et al. 2023, ApJL, 949, L23
Sun, G., Faucher-Giguère, C.-A., Hayward, C. C., & Shen, X. 2023, MNRAS, 526, 2665
Tacchella, S., Finkelstein, S. L., Bagley, M., et al. 2022, ApJ, 927, 170
Treu, T., Roberts-Borsani, G., Bradac, M., et al. 2022, ApJ, 935, 110
Trussler, J., Conselice, C., Adams, N., et al. 2024, MNRAS, 523, 3662
Trussler, J. A. A., Adams, N. J., Conselice, C. J., et al. 2023, MNRAS, 523, 3423
Trussler, J. A. A., Conselice, C. J., Adams, N. J., et al. 2025, MNRAS, 537, 3662
Vijayan, A. P., Lovell, C. C., Wilkins, S. M., et al. 2021, MNRAS, 501, 3289
Wang, B., Fujimoto, S., Labbé, I., et al. 2023, ApJL, 957, L34
Weaver, J. R., Taamoli, S., McPartland, C. J. R., et al. 2024a, ApJ, 964, 71
Weaver, J. R., Taamoli, S., McPartland, C. J. R., et al. 2024b, arXiv: 2405.13505
Whitaker, K. E., Ashas, M., Illingworth, G., et al. 2019, ApJS, 244, 16
Wilkins, S. M., Vijayan, A. P., Lovell, C. C., et al. 2023, MNRAS, 5189, 3118
Wilkins, S. M., Vijayan, A. P., Lovell, C. C., et al. 2023, MNRAS, 519, 3118
Williams, C. C., Curtis-Lake, E., Hainline, K. N., et al. 2018, ApJS, 236, 33
Williams, C. C., Spilker, J. S., Whitaker, K. E., et al. 2021, ApJ, 908, 54
Willott, C. J., Desprez, G., Asada, Y., et al. 2024, ApJ, 966, 74
Windhorst, R. A., Cohen, S. H., Jansen, R. A., et al. 2023, AJ, 165, 13
Yan, H., Cohen, S. H., Windhorst, R. A., et al. 2023, ApJL, 942, L8
Yung, L. Y. A., Somerville, R. S., Finkelstein, S. L., Wilkins, S. M., & Gardner, J. P. 2024, MNRAS, 527, 5929
Zavala, J. A., Castellano, M., Akins, H. B., et al. 2025, NatAs, 9, 155